Impacts of solar-absorbing aerosol layers on the transition of stratocumulus to trade cumulus clouds

Xiaoli Zhou[1], Andrew S. Ackerman[2], Ann M. Fridlind[2], Robert Wood[3] and
Pavlos Kollias[4,5]

1. Department of Atmospheric and Oceanic Sciences, McGill University, Montreal,
   Quebec, CA

2. NASA Goddard Institute for Space Studies, New York, New York, USA

3. University of Washington, Seattle, Washington, USA

4. School of Marine and Atmospheric Sciences, Stony Brook University, Stony Brook,
   New York, USA

5. Department of Environmental and Climate Sciences, Brookhaven National Laboratory,
   Upton, New York, USA

Correspondence to: Xiaoli Zhou (xiaoli.zhou@mail.mcgill.ca)

Abstract

The effects of an initially overlying layer of solar-absorbing aerosol on the transition of stratocumulus to trade cumulus clouds are examined using large-eddy simulations. For lightly drizzling cloud the transition is generally hastened, resulting mainly from increased cloud droplet number concentration (N_c) induced by entrained aerosol. The increased N_c slows sedimentation of cloud droplets and shortens their relaxation time for diffusional growth, both of which accelerate entrainment of overlying air and thereby stratocumulus breakup. However, the decrease in albedo from cloud breakup is more than offset by redistributing cloud water over a greater number of droplets, such that the diurnal-average shortwave forcing at the top of atmosphere is negative. The negative radiative forcing is enhanced by sizable longwave contributions, which result from the greater cloud breakup and a reduced boundary layer height associated with aerosol heating. A perturbation of moisture instead of aerosol aloft leads to greater liquid water path and a more gradual transition. Adding absorbing aerosol to that atmosphere results in substantial reductions in LWP and cloud cover that lead to positive shortwave and negative longwave forcings on average canceling each other. Only for heavily drizzling clouds is the breakup delayed, as inhibition of precipitation overcomes cloud water loss from enhanced entrainment. Considering these simulations as an imperfect proxy for biomass burning plumes influencing Namibian stratocumulus, we expect regional indirect plus semi-direct forcings to be substantially negative to negligible at the top of atmosphere, with its magnitude sensitive to background and perturbation properties.

1. Introduction

Aerosols affect the earth's radiation budget in at least three ways. First, they directly absorb and scatter solar radiation. Second, they affect radiative fluxes indirectly through their role as cloud condensation nuclei, influencing cloud microphysics and thereby affecting cloud albedo and cloud cover. Third, solar-absorbing aerosols can alter atmospheric heating rates and stability, leading to rapid adjustments in cloud properties; the resulting impact on radiative fluxes is referred to as the semi-direct effect (Hansen et al., 1997).

Aerosols have been identified as contributing the greatest uncertainty to anthropogenic climate forcing (Forster et al. 2007). For instance, the observational study of Indian Ocean Experiment (INDOEX) (Jayaraman et al., 1998; Satheesh and Ramanathan, 2000) and some general circulation model (GCM) studies (e.g., Hansen et al., 1997; Lohmann and Feichter, 2001; Jacobson, 2002; Cook and Highwood, 2004) have found a net decrease in low-level cloud cover when solar-absorbing aerosols are present, which corresponds to a positive radiative forcing at the top of the atmosphere (TOA) that tends to warm the climate system, while other observational studies (e.g., Loeb and Schuster, 2008; Wilcox et al., 2010; Adebiyi et al. 2015, hereafter A15) have found the opposite, in which the cloud cover increases. Some GCM studies (e.g., Menon et al., 2002, Penner and Zhang, 2003; Sakaeda et al, 2011) have found that the radiative forcing depends crucially on the height of the absorbing aerosol. To better constrain radiative forcing in climate models, a comprehensive understanding of regional cloud-aerosol interactions and the corresponding radiative forcings is of value.

Here we focus on warm (liquid-phase) clouds in the planetary boundary layer

24 (PBL). Higher-level clouds are not considered. Process-level understanding of the

25 physical mechanisms underlying indirect and semi-direct aerosol radiative forcings has

26 been largely advanced through studies with large-eddy simulation (LES) models and in

27 situ observations. Regarding aerosol indirect forcing, with all else equal (particularly

28 cloud cover and liquid water path), increased cloud droplet number concentration (N_c)

29 resulting from increased aerosol concentration (N_a) increases cloud optical thickness and

30 thus albedo, thereby exerting a negative radiative forcing at TOA (Twomey 1974, 1991).

31 For precipitating clouds, increasing N_c can reduce precipitation and thereby enhance

32 liquid water path (LWP) and cloud cover (e.g., Albrecht, 1989; Ackerman et al., 1993;

33 Pincus and Baker, 1994; Hindman et al., 1994). However, for clouds with little

34 precipitation, modeling studies indicate that increased N_c tends to reduce LWP and cloud

35 cover by increasing PBL entrainment (Ackerman et al., 2004; Wood et al., 2007;

36 Ackerman et al., 2009), which can dry the PBL and reduce LWP when the overlying air

37 is sufficiently dry (Randall, 1984). Such a tendency is consistent with satellite

38 observations of LWP reduction in ship tracks, on average (Coakley and Walsh, 2002). At

39 least three microphysical mechanisms have been found to play a role in the entrainment

40 increase. First, in what we shall refer to as the "sedimentation effect", increased N_c leads

41 to smaller droplets that fall more slowly, which increases the amount of cloud water

42 available for evaporative cooling during entrainment events, thereby strengthening

43 entrainment (Bretherton et al., 2007). Second, in what we shall refer to as the

44 "evaporation effect", smaller droplets increase the total surface area of cloud droplets,

45 accelerating evaporation and driving stronger entrainment (Xue et al., 2008). Third,

46 increased N_c also suppresses drizzle, enhancing convective intensity and entrainment (e.g.,

47   Stevens et al. 1998, Wood et al. 2007). Under dry overlying air, all three effects tend to

48   reduce cloud cover and LWP, leading to a positive radiative forcing. However, if the

49   entrained air is sufficiently moist, entrainment can be expected to increase LWP (Randall,

50   1984).

51   Aerosol semi-direct effects have been studied by Ackerman et al. (2000) in the

52   context of trade cumulus under a sharp inversion, in which absorbing aerosol within the

53   boundary layer increases solar heating in a manner that stabilizes the PBL, reducing the

54   moisture supply from the surface and the amount of cloudiness, leading to a positive

55   radiative forcing at TOA. More directly in such a scenario the relative humidity of the

56   PBL is reduced by enhanced solar heating, reducing cloudiness as originally found in

57   global model simulations by Hansen et al. (1997). In contrast, Johnson et al. (2004)

58   conducted large-eddy simulations of marine stratocumulus and found that an absorbing

59   aerosol immediately above the PBL (and not entrained) strengthens the inversion,

60   reducing entrainment and thereby increasing cloud cover, leading to a negative radiative

61   forcing, while they found the opposite (positive radiative forcing) for aerosol heating

62   within the PBL. That study was motivated at least in part by measurements of absorbing

63   aerosol from biomass burning advected from Africa over Namibian stratocumulus, where

64   biomass burning aerosol plumes may also be well separated from the PBL (Keil and

65   Haywood, 2003, Haywood et al., 2003b), a factor that has been found to be critical to

66   absorbing aerosol effects on cloud fraction (Feingold et al., 2005).

67   Further complexity arises when considering the possibility that absorbing aerosol

68   can act as cloud condensation nuclei (CCN) and thereby increase N_c, which was

69   neglected in the early studies of Johnson et al. (2004) and Feingold et al. (2005) and only

70   represented quite crudely by Ackerman et al. (2000), who simply imposed a sequence of

71   uniform N_c values in their simulations. Here we will consider both roles of absorbing

72   aerosol.

73   By considering two trade cumulus regimes, one transitional case with a sharp

74   inversion (ATEX) and a more downstream case with greatly reduced cloud cover

75   (BOMEX), Johnson (2005) found the semi-direct aerosol forcing to depend strongly on

76   the cloud regime, with the magnitude of the forcing increasing with (unperturbed) cloud

77   cover. This regime dependence is relevant to the stratocumulus-to-cumulus transition

78   (SCT), a climatological feature downstream of subtropical marine stratocumulus (Klein

79   and Hartmann, 1993; Sandu et al., 2010; Zhou et al., 2015). The SCT has been found in

80   modeling studies to be driven by easterly, equatorward advection over increasing sea

81   surface temperatures (SST), which increases surface latent heat fluxes, enhancing

82   buoyancy fluxes in the cloud layer and hence entrainment. The PBL deepening from

83   progressive entrainment inhibits the ability of circulations forced at cloud top to maintain

84   a well-mixed boundary layer, reducing the surface moisture supply and eventually drying

85   out the stratocumulus clouds (Bretherton and Wyant, 1997; Wyant et al., 1997). A recent

86   observational study has found that the time scale of the SCT over the eastern Pacific can

87   depart considerably from that in an idealized model framework driven only by increasing

88   SST (Zhou et al., 2015), suggesting that other factors, such as meteorological variability,

89   might play important roles in the time scale of SCT. Yamaguchi et al. (2015) (hereafter

90   Y15) investigated the impact of overlying absorbing aerosol and associated enhanced

91   moisture on the SCT and found that entrained absorbing aerosol in general delays the

92   SCT with a net negative change in TOA shortwave (SW) cloud radiative forcing (CRF).

93   It has been documented in recent observational studies near northern Namibia and

94   remote St. Helena Island in the South Atlantic that the sampled absorbing aerosol is often

95   accompanied by enhanced humidity, with an average moisture perturbation of ~1 g kg^{-1}

96   relative to the underlying air (Haywood et al., 2003b; A15). This humidity is associated

97   with the outflow from the deep, continental boundary layer, and accompanies the

98   absorbing aerosol that results from biomass burning. The enhanced humidity induces

99   additional radiative heating, which can regulate cloud processes by reducing cloud-top

100   longwave (LW) cooling (A15) and by simply reducing the dryness of air entrained into

101   the PBL. Y15 located a stationary moist layer above the PBL and found that the

102   additional moisture itself enhances cloud breakup during the SCT, although they

103   acknowledge that their perturbation of ~3 g kg^{-1} likely represents an upper limit

104   compared with A15. We note that in our modeling framework it is simply assumed that

105   the model domain is advected equatorward by the trade winds, thus implicitly treating the

106   flow aloft as being easterly, despite observations that indicate the circulation over the

107   South Atlantic to be far more complex (e.g., Adebiyi and Zuidema, 2016).

108   Here we perform an expanded investigation of the impact of absorbing aerosol

109   and moisture on the SCT. Because Y15 was published during the course of this work, our

110   simulation setups are similar but not identical, and we highlight similarities and

111   differences below. Like Y15, we adopt the Sandu and Stevens (2011) SCT case study,

112   with some modifications. Here we separate the responses to aerosol heating above and

113   within the PBL and on microphysical processes. We consider the impacts on lightly and

114   heavily drizzling stratocumulus decks. We also assess the impacts of additional overlying

115   moisture on the SCT and how it influences the effects of absorbing aerosol. The radiative

116 forcings in our study consider not only changes in SW but also LW fluxes. Our results

117 differ from Y15 in that initially overlying plumes of absorbing aerosol lead to positive

118 changes in SW CRF at TOA, and the aerosol and moisture perturbations never delay the

119 SCT in our simulations (unless we omit well-established physical processes).

120   The remainder of this manuscript is organized as follows. Section 2 documents

121 the model setup and case description. Section 3 presents analysis of the microphysical

122 and heating effects of absorbing aerosol during the transition of lightly drizzling

123 stratocumulus. In sect. 4, we investigate the impact of additional moisture in the aerosol

124 layer, and the influence of the initial altitude of the moist aerosol layer. The impacts of an

125 absorbing aerosol on the SCT of heavily drizzling stratocumulus are discussed in sect. 5.

126 In sect. 6 we discuss and summarize our findings.

127

128 **2. Model setup and simulated cases**

129   The Distributed Hydrodynamic Aerosol and Radiative Modeling Application

130 (DHARMA) (Ackerman et al., 2004 and references therein) simulations here are based

131 on the "reference case" 3-day Lagrangian SCT setup of Sandu and Stevens (2011). The

132 basis for the case is a composite of the large-scale conditions encountered along

133 trajectories over the northeast Pacific from June to August of 2006 and 2007. Following

134 Sandu and Stevens (2011) and de Roode et al. (2016), SST increases steadily from 293.75

135 K at 0 h to 299.17 K at 72 h, and a uniform divergence of large-scale horizontal winds of

136 1.86×10^{-6} s^{-1} is imposed up to an altitude of 2000 m, above which the large-scale

137 subsidence is constant. Because the large-scale subsidence is imposed rather than

138 interactive, we omit any possible decrease in subsidence associated with solar heating by

139 absorbing aerosol (cf. Sakaeda et al. 2011). An intercomparison of six different LES

140 models shows that DHARMA results are consistent with others in representing the SCT

141 (de Roode et al., 2016), although differences between models do exist, as discussed

142 further below. Unlike Sandu and Stevens (2011) and Y15, here we begin simulations at

143 midnight local time (when turbulent mixing is vigorous, to accelerate spin-up) rather than

144 10:00 local time. Surface fluxes are computed following similarity theory as in Ackerman

145 et al. (1995). Note that because sea surface temperature is prescribed, it is not impacted

146 by changes in the overlying atmosphere.

147   The DHARMA domain size is 10.8 km x 10.8 km x 3.2 km and horizontal

148 resolution is set to $\Delta x = \Delta y = 75$ m. Vertically 240 levels are distributed between 0 and

149 3200 m, with variable vertical resolution ranging from 30 m near the surface to 10 m near

150 the inversion and up to 60 m near the model top; before using this grid with twice as

151 coarse of a grid as in de Roode et al. (2016), we confirmed that the DHARMA results

152 were not sensitive to the difference. The microphysics scheme is an adaptation of the

153 two-moment scheme of Morrison et al. (2005) with prognostic saturation excess

154 following Morrison and Grabowski (2008) and assuming the shape factor of the cloud

155 droplet size distribution to be 10.3 (equivalent to relative dispersion of 0.3) following

156 Geoffroy et al. (2010). Radiative transfer is calculated for each column every minute

157 using a two-stream model (Toon et al., 1989). An isothermal layer for the radiative

158 transfer calculations overlies the LES grid, with an ozone column following the

159 specifications of de Roode et al. (2016) and with temperature (180 K) and water vapor

160 column (0.5 g cm^{-2}) chosen to match the profile of downwelling LW flux of the other

161 models in the intercomparison. The ocean surface albedo is spectrally uniform at 7%.

162   Activation of aerosol follows Abdul-Razzak and Ghan (2000) using supersaturation

163   computed after the condensational adjustment of Eq. A10 in Morrison and Grabowski

164   (2008). The number and mass concentrations of cloud droplet and raindrops are

165   prognostic in the two-moment cloud microphysics scheme, but for aerosol it is only the

166   number concentration of unactivated plus activated particles for each aerosol species that

167   is prognostic; there is no evolution of the size and breadth of the underlying aerosol size

168   distribution for each species, nor are there sources or sinks of aerosol number.

169   Two species of aerosol are prescribed: ammonium sulfate and a solar-absorbing

170   aerosol; both aerosol types act as CCN and interact with the radiation before and after

171   activation. The optical properties for aerosol particles and hydrometeors are computed

172   following Ackerman et al. (1995) using Mie calculations on a 25-bin grid with geometric

173   spacing, in which we average over six sub-intervals within each bin to smooth any Mie

174   resonances. Soot cores with a fixed size are included in the Mie calculations for solar

175   absorbing aerosol (following Ackerman et al., 2000) as well as for the fraction of cloud

176   droplets in each grid cell that activated on solar absorbing CCN. The baseline case is an

177   ensemble of three simulations with different pseudo-random seeds for the initial

178   temperature perturbation field in the PBL, and includes only ammonium sulfate aerosol,

179   which are uniformly distributed in the vertical with $N_{a, \text{sulfate}} = 150$ mg^{-1} (without a vertical

180   gradient the aerosol scheme is completely diagnostic). Further simulations are conducted

181   that incorporate an absorbing aerosol profile initialized to increase linearly from zero

182   below 1250 m altitude up to $N_{a, \text{absorb}} = 5000$ mg^{-1} at 1300 m, maintain a uniform value up

183   to 2800 m, then decrease to zero at 2850 m and above. Log-normal size distributions are

184   specified for the sulfate and absorbing aerosol, with geometric mean radii of 0.05 µm and

185   0.12 μm and geometric standard deviations of 1.2 and 1.3, respectively. The

186   hygroscopicity parameter κ (Petters and Kreidenweis, 2007) is set to 0.55 for ammonium

187   sulfate and 0.2 for the absorbing aerosol. The size distribution for the absorbing aerosol is

188   based on the measurements of Haywood et al. (2003b) and the hygroscopicity (for aged

189   biomass burning aerosol) from those of Englehart et al. (2012). The absorbing aerosol

190   optical properties follow the approach of Ackerman et al. (2000) but here a soot core

191   radius of 0.04 μm is specified, resulting in a single scattering albedo (SSA) of 0.88 at

192   wavelength 0.55 μm. The extinction coefficient within the absorbing aerosol layer is

193   about 0.16 km^{-1} at 0.55 μm, consistent with the measurements reported by Haywood et al.

194   (2003a). The absorbing aerosol induces a heating rate of ~2.6 K d^{-1} at noon and a diurnal-

195   average heating rate ~1.2 K d^{-1}, consistent with observations exploited by Johnson et al.

196   (2004) and Ackerman et al. (2000). The initial absorbing aerosol layer physical thickness

197   of 1.5 km is loosely based on observations over the southeast Atlantic by Chand et al.

198   (2009), Haywood et al. (2003b), and Labonne et al. (2007), who report characteristic

199   layer thickness over the Atlantic of 1 to 2 km. Sensitivities of the results to the assumed

200   SSA of the absorbing aerosol and to their initial number concentration are briefly

201   discussed.

202   To examine variations in bulk properties of the overlying aerosol layer, a further

203   simulation is performed with the initial location 400 m higher, in which the model top is

204   extended to 3.5 km and the column of overlying water vapor and ozone used for radiative

205   fluxes adjusted accordingly. An additional baseline case with a 3.5-km deep grid was run

206   for computing differences. Two other simulations consider a moist perturbation of 1 g kg^{-}

207   ^{1} based on observations at St. Helena Island of equatorward outflow from the continental

208   boundary layer (A15), scaled to the initial height of $N_{a,\,absorb}$ with and without absorbing

209   aerosol. Finally, the impact of overlying absorbing aerosol on heavily precipitating

210   stratocumulus is examined by reducing $N_{a,\,sulfate}$ to 25 mg^{-1}. To isolate the microphysical

211   effects of the overlying aerosol, a group of simulations with $N_{a,\,sulfate} = 150$ mg^{-1} is

212   performed where the interaction of the absorbing aerosol with radiation is omitted. The

213   aforementioned sedimentation and evaporation effects are examined by additional

214   simulations that exclude cloud droplet sedimentation and that fix the cloud droplet

215   relaxation time scale (instead of computing it per Equation A5 of Morrison and

216   Grabowski, 2008). Semi-direct aerosol effects are dissected through simulations that

217   restrict aerosol heating to the free troposphere (FT) or the PBL. Table 1 summarizes the

218   setups for all simulations in the main text and its last column lists the figures in which

219   each simulation appears.

220   Radiative forcings are computed from hourly time slices, which yield daily

221   averages that differ negligibly from those using radiative fluxes updated every minute.

222   We compute aerosol forcings following Ghan (2013), in which total forcing from a

223   perturbation is calculated as the change in net downward radiative flux at TOA relative to

224   the baseline: $\Delta F = F(\text{perturbed}) - F(\text{baseline})$. The sum of the indirect and semi-direct

225   forcings from the absorbing aerosol is computed similarly but with the absorbing aerosol

226   omitted when calculating $F(\text{perturbed})$. The direct aerosol forcing is then derived by

227   subtracting the sum of indirect and semi-direct forcings from the total forcing.

228   For the sake of comparison with Y15, in one instance we also compute cloud

229   radiative forcing as the difference of net downward radiative fluxes at TOA with and

230   without cloud: $F(\text{all sky}) - F(\text{clear sky})$. The difference between ΔF and the aerosol-

231   induced change in cloud radiative forcing is the direct aerosol forcing for clear sky:

232    $\Delta CRF = \Delta F - \Delta F$(clear sky). The enhancement of aerosol absorption associated with SW

233   reflection by an underlying cloud layer, which tends toward a positive forcing (e.g.,

234   Chand et al., 2009) and is implicitly included in ΔF, is offset in ΔCRF by the subtraction

235   of a direct forcing that tends more negative here, because the ocean surface is less

236   reflective than the cloud layer. Subtraction of a negative direct forcing thereby yields a

237   ΔCRF that tends to be more positive than total forcing ΔF.

238   In all forcing calculations for this study, net LW fluxes at TOA are scaled from

239   net LW fluxes at the top of the model domain using $F_{\mathrm{TOA}} = 2.627 F_{3.2\mathrm{km}} + 0.0054 F_{3.2\mathrm{km}}^{2}$

240   for the 3.2-km deep grid, and using $F_{\mathrm{TOA}} = 2.469 F_{3.5\mathrm{km}} + 0.0046 F_{3.5\mathrm{km}}^{2}$ for the 3.5-km

241   deep grid. These correlations were derived from the baseline case run on a 40-km deep

242   grid, with root mean square (RMS) errors of 0.3 and 0.2 W m^{-2} on the shallower grids,

243   with biases of less than 0.001 W m^{-2}. No TOA corrections for SW fluxes are made

244   because the radiative transfer scheme (Toon et al., 1989) provides accurate TOA fluxes

245   by treating Rayleigh scattering in the overlying atmosphere.

246

247   **3. Impacts on lightly drizzling SCT**

248   **3.1.   Overview of SCT with and without absorbing aerosol layer**

249   Figs. 1 and 2 illustrate the transition from a compact stratocumulus layer to more

250   broken fields of cumulus as a response to increasing SST for the lightly drizzling baseline

251   case ($N_{a,\,\mathrm{sulfate}} = 150$ mg^{-1}, $N_c \sim 100$ cm^{-3}). After ~ 2 h of boundary layer turbulence spin-

252   up in one member of the baseline ensemble (Fig. 1b), the PBL depth in general

253   increases with SST and reaches 2 km at the end of day 3 (Fig. 1a). The thinning of the

254   stratocumulus is observed in the afternoon of day 1 as solar heating offsets some of the

255   LW cooling that drives PBL mixing, when vertical wind variance profiles show bimodal

256   structure with a local minimum near cloud base (~12 h in Fig. 1b). Convection revitalizes

257   after sunset and deepens the stratocumulus, when the mean precipitation rate at cloud

258   base peaks at ~0.1 mm d^{-1} in the baseline ensemble (Fig. 2i). Starting around sunrise of

259   day 2 (~30 h), the PBL becomes continuously stratified, with a persistent cumulus layer

260   developing under the stratocumulus (Fig. 1a). This stratification reduces the subsequent

261   nocturnal recovery, and leads to further reduction in LWP (Fig. 2b) and cloudiness (Fig.

262   2c) after sunrise on day 3. Following Sandu and Stevens (2011) by defining the SCT as

263   the time at which cloud cover (the fraction of columns with LWP > 10 g m^{-2}) first

264   decreases to half of its initial value, the transition in the baseline case is at ~62 h.

265   When incorporating an overlying absorbing aerosol layer, the clouds and PBL

266   evolve in a notably different way with an evident radiative impact (Figs. 2 and 3; Table 2).

267   N_c increases gradually after the bottom of the ramp of subsiding aerosol contacts the

268   deepening PBL at ~15 h (Fig. 2a). The full strength of the aerosol layer reaches the PBL

269   at ~20 h (Fig. 2d). Before the subsiding aerosol layer contacts the deepening PBL,

270   absorption of SW radiation in the aerosol layer dominates the radiative impact and

271   reduces the diurnal-average upwelling SW radiative fluxes at TOA by ~7 W m^{-2} on day 1

272   (Fig. 2f, Table 2). This SW absorption by the aerosol layer decreases with time when the

273   cloud field is more broken, since less upwelling SW radiation is reflected back into the

274   layer (cf. Chand et al., 2009) and when it is mixed below cloud, where less SW radiation

275   reaches the absorbing aerosol. On day 3, SW absorption is overcome by scattering,

276   resulting in a negative direct forcing (Table 2).

277   As the absorbing layer approaches the PBL, the inversion strengthens (Fig. 2h),

278   which would tend to slow entrainment. However, as the layer makes contact with the

279   clouds, the entrained aerosol activate cloud droplets and lead to a pronounced increase of

280   N_c, which is ultimately increased by a factor of ~10 over the baseline to ~1000 cm^{-3} (Fig.

281   2a). The increased N_c acts to accelerate entrainment through the sedimentation and

282   evaporation effects, and opposes but does not overcome the opposing tendency from the

283   strengthening of the inversion (Figs. 2d and 2e). The entrainment of warmer air with less

284   RH leads to a reduction of LWP (Fig. 2b) and cloud cover (Fig. 2c), hastening and

285   enhancing the SCT on day 2 (Fig. 2c). This SCT acceleration is opposite to Y15 who

286   found that entrained absorbing aerosol delays the SCT and leads to overcast conditions

287   during the second half of 72-h simulations. As a result of substantially reduced LWP,

288   here the overlying absorbing aerosol case yields a positive change in TOA SW CRF

289   relative to the baseline during the 3-day simulation (Table 3). The daytime average SW

290   ΔCRF after the soot contacts the PBL is 9.3 W m^{-2}, opposite in sign to that of Y15.

291   Meanwhile, the negative LW contributions to ΔCRF are enhanced during the transition,

292   and overcome the positive SW ΔCRF on day 3. As explained further below, such LW

293   contributions result from microphysical and heating effects. While such LW forcings are

294   often ignored when considering aerosol impacts on low-lying clouds, much of the

295   subtropical and tropical atmosphere is not particularly moist, with column water vapor of

296   less than 30 mm (cf. Lindstrot et al. 2014) as it is here (initial and final values

297   respectively about 25 and 30 mm), allowing changes in low-level clouds to impact LW

298   fluxes at TOA.

299

300   **3.2 Microphysical effects**

301   The microphysical effects of the subsiding aerosol are isolated by omitting aerosol

302   heating and comparing to the same baseline (Fig. 4). The substantial increase of N_c as a

303   result of the entrained aerosol is seen to largely explain overall reductions of both LWP

304   and cloud cover relative to the baseline simulation, leading to a hastened SCT. Such

305   disparity in LWP and cloud cover with and without entrained aerosol is reduced when

306   either the sedimentation effect is excluded (by omitting cloud droplet sedimentation from

307   both simulations) or when the evaporation effect is excluded (by fixing the cloud droplet

308   diffusional growth relaxation time in both simulations). When both effects are excluded,

309   simulations with and without entraining aerosol exhibit negligible differences in LWP

310   and a reversed difference in cloud cover. Thus, the hastened SCT from absorbing aerosol

311   in DHARMA simulations can be attributed primarily to the microphysical effects of

312   increased N_c, specifically via sedimentation and evaporation effects.

313   With the semi-direct effect now excluded by omitting aerosol absorption, the

314   indirect forcing is isolated (Table 4). Despite the substantial reduction in cloud cover, the

315   entrained aerosol results in only a modest positive aerosol indirect forcing on day 2 and a

316   negative forcing on day 3 (Table 4). The negative forcing is driven by a negative LW

317   forcing, as a result of more broken clouds and emission from a warmer SST, and by a

318   significant Twomey effect, which does not fully offset the opposed, comparable SW

319   forcing induced by the sedimentation and evaporation effects (Table 5).

320

321   **3.3 Semi-direct effects**

322   Next we isolate the semi-direct effects of aerosol heating by considering aerosol

323   absorption in the FT, PBL and throughout the atmosphere and comparing to the

324   preceding case that only included microphysical effects of the entrained aerosol layer. By

325   doing so we build upon the results of the previous section, effectively evaluating the

326   semi-direct effect in the presence of microphysical effects rather than in their absence. As

327   seen in Fig. 5, aerosol heating in the FT substantially strengthens the PBL inversion as

328   the aerosol layer approaches the PBL (Fig. 5e), enhancing LWP and cloud cover (Figs. 5b

329   and 5c) by inhibiting entrainment (Fig. 5d). The increase of LWP delays and weakens the

330   SCT, contributing to a negative SW forcing (Table 6). In contrast, aerosol heating in the

331   PBL reduces LWP and cloud cover in the daytime (Figs. 5b and 5c) by lowering the

332   relative humidity in the PBL and by stabilizing the PBL (Fig. 6a), hampering the

333   moisture supply from the surface (Fig. 6b). The reduction in cloud amount amplifies the

334   diurnal contrast of cloud fraction and hastens the SCT, resulting in a positive SW forcing

335   (Table 6).

336   The competing effects of aerosol heating in the FT versus the PBL serve to

337   increase cloud water at night while reducing it during daytime, enhancing its diurnal

338   cycle (Fig. 5c). Diurnally averaged, the effect of aerosol heating in the FT is dominant

339   and leads to increased LWP and cloud cover and therefore a negative average SW forcing

340   during the 3-day transition (Fig. 5c, Table 6). The net SW forcing is smaller than the sum

341   of the SW forcings via individual FT and PBL aerosol heating, indicating interactions

342   that reduce the component forcings when combined (Table 6). Specifically, aerosol

343   absorption in the FT slightly reduces the SW flux available for aerosol heating in the PBL,

344   while the greater cloud breakup in the daytime reduces the reflected upwelling SW flux,

345   in turn reducing aerosol heating in the FT. The combined effects also result in LWP and

346   cloud cover intermediate between the results when considered separately (Fig. 5).

347   In contrast to the counteracting impacts on cloud water, FT and PBL aerosol

348   heating both inhibit entrainment by intensifying the inversion and by stratifying the PBL

349   (Fig. 5c). The reduced PBL depth corresponds to warmer cloud tops, which emit more

350   LW radiation upwards, leading to net negative LW forcing on days 2 and 3 despite an

351   increase of LWP and cloud cover (Table 6).

352

353   **3.4. Combined effects**

354   Comparing Tables 2, 4 and 6 it is seen that net SW forcing is weakened with all

355   effects included because the increased LWP from aerosol heating compensates for some

356   of the LWP loss from microphysical effects on day 2 (Table 2, Fig. 6), and the direct

357   aerosol heating on day 1 greatly counteracts the negative radiative forcings after the

358   aerosol layer contacts the PBL. As a result, the mean SW impact over the 3-day transition

359   nearly vanishes (Table 2). The LW radiative forcing, however, accumulates and

360   strengthens during the transition, and therefore is the dominant contributor to a negative

361   average forcing during the transition (Table 2). In a nutshell, although the subsiding

362   aerosol layer directly absorbs solar radiation and breaks up the clouds faster and more

363   thoroughly, the CCN source serves to distribute cloud water over a greater number of

364   drops, increasing the optical thickness of the remaining clouds but at a lower altitude,

365   increasing both upwelling SW and LW radiative fluxes, leading to a net negative forcing.

366   We note that day 3 net SW forcing is only negative when the aerosol is absorbing

367 (-1.2 W m^{-2} in Table 2); otherwise, the Twomey effect is not strong enough to counteract

368 the reduction in cloud fraction and day 3 net SW forcing is equally positive (1.2 W m^{-2} in

369 Table 4).

370   The study of the effects of absorbing aerosol on the SCT by Y15 considered only

371 SW forcings, which seems sensible given that studies of semi-direct effects in

372 stratocumulus (Johnson et al., 2004) and trade cumulus (Ackerman et al., 2000; Johnson,

373 2005) have found SW forcings to be dominant. However, here we find interactions of

374 aerosol and clouds in response to multiple effects leads to small net SW forcings: for

375 example, positive SW forcing from PBL aerosol heating and microphysical effects on

376 dynamics offset negative SW forcing from FT aerosol heating and the Twomey effect

377 (Table 5). By contrast, the negative LW forcings from multiple effects (i.e., cloud water

378 reduction and PBL deepening) work in the same direction and result in a substantial net

379 LW forcing for the SCT.

380   Sensitivity tests with varying values of the SSA and initial number concentration

381 of the absorbing aerosol are summarized in Appendix A1. A decrease of SSA at 0.55-μm

382 wavelength from 0.88 to 0.71 hastens the SCT less but leads to a positive radiative

383 forcing averaged over the 3-day transition, attributable to direct absorption by the aerosol.

384 A decrease of the initial number concentration for the overlying aerosol with SSA of 0.88

385 serves to weaken its negative 3-day average radiative forcing.

386

387 **4 Variations in bulk properties of overlying aerosol layer**

388 **4.1. Higher initial elevation**

389   Increasing the initial height of the base of aerosol layer by 400 m delays contact

390 with the PBL by about half a day (Fig. 7a). The delayed contact reduces the entrainment

391 of aerosol relative to the case with the layer starting lower, thereby hindering cloud

392 breakup (comparing Figs.7b-c with Figs. 2b-c). The enhanced cloud amount leads to a

393 much greater SW negative forcing on days 2 and 3, despite greater direct absorption

394 owing to the extended duration of the aerosol aloft on day 2 (2 and 7). The delayed

395 contact also provides for a longer duration of heating aloft and thereby a stronger

396 inversion on day 3 (Fig. 7e), favoring maintenance of the clouds and thus a negative SW

397 forcing. Despite increased LWP and cloud cover, the SCT with a higher elevated aerosol

398 layer is still hastened relative to the baseline (Fig. 7). The greater negative SW forcing of

399 the more elevated aerosol layer after its contact with the PBL ultimately leads to a more

400 negative 3-day mean radiative forcing to the case with the layer starting lower (Tables 2

401 and 7).

402

403 **4.2. Additional moisture**

404   Given that observations indicate that biomass burning plumes over Namibian

405 stratocumulus are moister than the surrounding air (A15), next we additionally consider a

406 moisture perturbation relative to the baseline. As seen in Fig. 8, the moisture induces

407 additional SW heating and LW cooling (Figs. 8a, b), with the latter dominating. The net

408 cooling offsets some SW heating especially near the top of the moist layer (Fig. 8c).

409 Before the moist layer contacts the PBL, the additional downward LW radiative fluxes

410   from its moisture serve to reduce cloud-top radiative cooling and thereby drive weaker

411   PBL mixing that results in a more broken cloud field relative to the dry case (Fig. 9c).

412   Reduced LWP diminishes upwelling SW radiative fluxes, enhancing the positive SW

413   forcing on day 1 (Table 8). After the moist layer contacts the PBL, the entrained moist air

414   leads to greater LWP and cloud cover than for the baseline, despite a weaker inversion

415   (Figs. 8c and 9e). The increased cloud water greatly increases the net outgoing SW flux at

416   TOA on days 2 and 3 (Table 8), and delays the SCT relative to the dry baseline (Figs. 9b

417   and 9c). The SW changes in TOA radiative fluxes are seen in Table 8 to dominate the

418   LW changes.

419   When an absorbing aerosol is then added to the moist layer aloft, the SCT is faster

420   and more pronounced relative to the case with only a moisture perturbation (Fig. 9c).

421   Comparison of Tables 2 and 9 reveals that the LW forcings are comparable with and

422   without the additional moisture, but the SW forcings induced by indirect and semi-direct

423   effects are about 4 W m^{-2} greater on days 2 and 3 with the moisture aloft. A thicker cloud

424   layer with greater cloud cover has more to lose, and the more dramatic reduction in cloud

425   cover during daytime predominantly changes the SW forcing. During nighttime, however,

426   cloud cover diminishes less as a result of the entrained moist air (Fig. 9c). The

427   counteracting day and night impacts on cloud cover keep the PBL depth close to that in

428   the absence of the additional moisture (Fig. 9d), leading to little difference in the diurnal

429   average LW forcing (Fig. 9f, Table 9). The net result averaged over the 3-day transition is

430   a modest positive SW forcing that cancels out the negative LW forcing (Table 9).

431

5. Impacts on heavily drizzling stratocumulus

The background aerosol concentrations in our simulations result in negligible drizzle for these conditions. As SCT is often observed in association with precipitation (e.g., Zhou et al., 2015), we next consider the impact of absorbing aerosol on the SCT of heavily drizzling stratocumulus by reducing the $N_{a,\,sulfate}$ by six-fold, to 25 mg^{-1}. Throughout this section the aerosol layer base is initially at 1.3 km and the layer does not include additional moisture.

The reduced $N_{a,\,sulfate}$ is associated with domain-mean drizzle at cloud base reaching ~2 mm d^{-1} each night (Fig. 10f). With drizzle the stratocumulus deck retains the essential features of the PBL growth and of the thinning and dissipation of the stratocumulus layer during the SCT, but exhibits differences associated with a much weaker diurnal cycle (Fig. 10), as also reported by Sandu and Stevens (2011). As discussed in Sandu et al. (2008), a weaker diurnal cycle is attributable to depletion of cloud water and stratification of the PBL via precipitation, which limits the stratocumulus invigoration during the night. A reduced LWP in turn lessens solar heating after sunrise, reducing daytime cloud thinning and breakup.

As seen in Fig. 10f, entrainment of aerosol inhibits drizzle and thereby thickens the stratocumulus layer. This inhibition of drizzle restores more than enough cloud water to overcome PBL drying tendencies from the increased entrainment on day 2. After sunrise, cloud cover falls sharply as the reduced drizzle strengthens the diurnal cycle. Owing to a thicker nocturnal cloud deck and a stronger inversion from aerosol heating aloft, cloud breakup is delayed but amplified on day 2. On day 3, the aerosol heating in the presence of a stronger diurnal cycle results in a hastened SCT.

455   The inhibition of drizzle on day 2 allows for greater mixing and entrainment (cf.

456   Stevens et al., 1998) despite the stronger inversion from aerosol heating aloft (Fig. 10d).

457   The deeper PBL is associated with cooler cloud tops that emit less LW radiation, leading

458   to a positive LW forcing during the transition (Table 10). Such positive LW forcing is

459   more than offset by the strong SW forcing attributable to a strong Twomey effect

460   (relative to a cleaner baseline for this heavily drizzling case), and the net impact is

461   therefore an amplified negative forcing (Table 10).

462

463   **6. Discussion and conclusions**

464   In this study we have examined the impact of an initially overlying layer of

465   absorbing aerosol on the stratocumulus-to-cumulus transition (SCT) of lightly and

466   heavily drizzling clouds via large-eddy simulations. Our results indicate that the

467   overlying aerosol can profoundly modify the breakup of stratocumulus as it advects over

468   increasingly warm SSTs. During the transition of lightly drizzling clouds, an overlying

469   absorbing aerosol results in a more broken cloud field, hastening the SCT and

470   strengthening the diurnal cycle. The hastened SCT in our simulations is primarily

471   attributable to an increased number concentration of cloud droplets leading to faster

472   evaporation of more cloud water that enhances entrainment. This result holds in the

473   presence of additional moisture in the aerosol layer and is insensitive to a 400-m increase

474   in its initial altitude. Drizzle constitutes another degree of complexity. Its inhibition from

475   aerosol entrainment thickens the stratocumulus and leads to a stronger diurnal cloud cycle

476   that ultimately hastens the SCT.

477   The hastening of the SCT in this study is notable in contrast with Y15, who found

478   the opposite in a similar study. The entrained aerosol in that study leads to increased

479   cloudiness and a delay of the SCT before precipitation develops, suggesting that

480   inhibition of precipitation is not the cause of delayed SCT in Y15. The strength of

481   sedimentation and evaporation effects in the Y15 simulations are not obvious; we do find

482   a delay in the SCT for a lightly drizzling case only when sedimentation and evaporation

483   effects are both omitted (see Appendix A2). It is noteworthy that direct numerical

484   simulation (DNS) indicates that the sensitivity of cloud-top entrainment is substantially

485   underpredicted in LES (de Lozar and Mellado, 2016), so in reality the microphysical

486   effects may be considerably stronger than represented here. Another likely source of

487   discrepancy between our studies could be differences in model formulations. Y15 use the

488   System for Atmospheric Modeling (SAM; Khairoutdinov and Randall, 2003) whereas

489   here we use DHARMA (Ackerman et al., 2004). As seen in the intercomparison of de

490   Roode et al. (2016), the evolution of cloudiness in SAM and DHARMA for that study's

491   reference case (after Sandu and Stevens, 2011, from the observational study of Sandu et

492   al., 2010) is notably different in that DHARMA tends to ultimately develop a more

493   broken cloud field than SAM. The cloud cover in DHARMA better resembles the

494   satellite observations of Sandu et al. (2010) than SAM does during the SCT (Fig. 3k in de

495   Roode et al., 2016), but that is not necessarily proof of model skill since case study large-

496   scale forcings tend to be insufficiently constrained by available observations (e.g.,

497   Vogelmann et al. 2015). Whereas here we neglect consumption of aerosol number

498   (activation into cloud droplets is reversible through evaporation) owing to an absence of

499   constraints on aerosol source terms. In contrast, Y15 include aerosol consumption, and a

500 fixed surface source, which together result in their in-cloud droplet number concentration

501 dropping rapidly to $O(10 \text{ cm}^{-3})$ within the final 12 h of their control simulation, inducing

502 a dramatic decrease in cloud cover that does not occur when an overlying aerosol layer is

503 included. The detailed dynamical and microphysical differences between the studies

504 warrant further investigation, and future observational studies are necessary to provide a

505 firmer foundation for establishing the impact of absorbing aerosol on the timing of SCT.

506   Our study suggests that even in the case of a hastened transition an initially

507 overlying absorbing aerosol layer can produce net negative aerosol indirect and semi-

508 direct radiative forcings during SCT. For lightly drizzling stratocumulus, such negative

509 forcing is mainly attributable to greater cloud albedo from a dominant Twomey effect and

510 to negative LW forcing from greater cloud breakup over warmer SSTs and reduced PBL

511 top height from aerosol heating. Diminishing already from the interactions between

512 microphysical and semi-direct processes, when combined with aerosol direct SW forcing,

513 the net SW forcing nearly vanishes, thus becoming even less significant relative to the

514 negative LW forcing during the SCT. We recommend that such sizable LW forcings not

515 be neglected when considering semi-direct aerosol forcings in the context of

516 stratocumulus breakup. Further sensitivity tests (Appendix A1) show that when SSA at

517 0.5-μm wavelength decreases further, the negative contributions can be overcome by the

518 large positive SW forcing via direct absorption, leading to net positive aerosol forcings.

519 We find it likely that similar positive forcings occur with an increase of aerosol layer

520 thickness.

521   When the aerosol layer is initially placed at a higher altitude, the extended

522 duration of aerosol overriding the stratocumulus deck intensifies the positive SW forcing

523 from direct absorption, while largely enhancing the negative SW indirect and semi-direct

524 forcings from less LWP reduction owing to less entrained aerosol and a stronger

525 inversion, leading to a more negative net forcing when averaged over the 3-day transition.

526   A moist layer aloft associated with outflow from a deeper continental PBL tends

527 to intensify the radiative forcings by reducing cloud-top LW cooling and thus convective

528 intensity and increasing the positive SW forcing before contact with the PBL, and by

529 enhancing negative SW forcing after contact via greater LWP resulting from reduced

530 PBL drying. The net effect of the overlying additional moisture is to modestly increase

531 cloud water during the 3-day transition. Absorbing aerosol in the presence of additional

532 moisture tends to break up the cloud more dramatically relative to the effect of absorbing

533 aerosol without additional moisture aloft. The presence of moisture little affects the LW

534 forcing but leads to substantially more net downward SW flux at TOA. Averaged over

535 the 3-day transition, the positive SW forcing cancels out the negative LW forcing.

536   We note that the simulations in this study are derived from observations over the

537 northeast Pacific Ocean (Sandu et al., 2010) whereas the characteristics of the overlying

538 absorbing aerosol layer are based on observations from the southeast Atlantic (A15). The

539 different large-scale meteorological conditions at these two locations may limit the

540 generality of this study to the SCT over the Atlantic. However, we find it likely that

541 similarly complex interactions (as summarized in Table 4) do occur. Future LES and

542 global modeling studies based on conditions over the southeast Atlantic should be

543 developed to evaluate the results presented here and in Y15. This study may help inform

544 future analyses primarily by emphasizing the complexity of competing LW and SW

545 effects, and giving some indication of their relative strengths, which lead to a wide range

546   of indirect plus semi-direct forcings from slightly positive to –20 W m^{-2} over our 3-day

547   simulations, depending upon assumptions made (Tables 2, 9, 10, and A1). The duration

548   of time before the absorbing aerosol layer makes contact with the PBL, the strength of

549   drizzle prior to contact, the number concentration of aerosol entrained after contact and

550   the amount of moisture accompanying the aerosol are all found to be factors of leading

551   potential importance to regional radiative impacts of biomass burning over the southeast

552   Atlantic and elsewhere.

553

554   *Acknowledgments*. This research was funded by the NASA ORACLES project

555   and the DOE ASR program. Resources supporting this work were provided by the NASA

556   High-End Computing (HEC) Program through the NASA Advanced Supercomputing

557   (NAS) Division at Ames Research Center. We thank Paquita Zuidema and an anonymous

558   reviewer for helpful suggestions.

559   APPENDIX

560   **a. Sensitivity to single scattering albedo of absorbing aerosol**

561   Fig. A1 compares the 3-day transition with varying values of single-scattering albedo

562   (SSA, at 0.55-μm wavelength) for the absorbing aerosol. As discussed earlier, the

563   microphysical effect of aerosol acts to greatly reduce cloud water and hasten the SCT by

564   virtue of enhanced entrainment. This effect is also seen in the "SSA=1" case (no

565   absorption) in Fig. A1. The increased entrainment is reflected by the fact that the

566   deepening of the PBL varies little from the baseline simulation, despite substantially

567   reduced cloud cover and LWP. A decrease of SSA from 1 to 0.88 (the value used for the

568   absorbing aerosol throughout the study) serves to strengthen the inversion and enhance

569   the diurnal cycle. These trends are greater when SSA is further reduced to 0.71, which

570   strengthens the inversion by ~3 K on day 2 and ~4 K on day 3, and deepens the PBL 400

571   m less by the end of day 3. The strengthened inversion slightly hinders cloud breakup,

572   while still hastening the SCT relative to the baseline (Figs. A1b and A1c). Although the

573   decrease of SSA amplified the net negative LW forcing via the slower deepening of the

574   PBL, that LW forcing is more than offset by the positive SW forcing attributable to direct

575   absorption by the aerosol, and therefore the 3-day mean radiative forcing increases with

576   the decrease of SSA. Thus, for the strongly absorbing aerosol case (SSA = 0.71) it is seen

577   in Table A1 that the net radiative forcing is positive on average.

578

579   **b.   Combined effects of overlying absorbing aerosol in the absence of**

580   **sedimentation and evaporation effects**

581   As seen in Fig. A2, an overlying absorbing aerosol results in a delayed SCT when

582   sedimentation and evaporation effects are both omitted. The lack of microphysical

583   effects on dynamics isolates the influence of aerosol heating, which increases LWP

584   and especially cloud cover during the night and delays the SCT. We note that Y15

585   also found a delay in the SCT, but the similarity with this result may be coincidental.

586

587   REFERENCES

588   Abdul-Razzak, H., & Ghan, S. J. (2000). A parameterization of aerosol activation 2. Multiple aerosol types.

589   *J. Geophys. Res., 105*, 6837-6844.

590   Ackerman, A. S., Toon, O. B., & Hobbs, P. V. (1993). Dissipation of marine stratiform clouds and collapse

591   of the marine boundary layer due to the depletion of cloud condensation nuclei by clouds. *Science*,

592   *262*(5131), 226-229.

593   Ackerman, A. S., Hobbs, P. V., & Toon, O. B. (1995). A model for particle microphysics, turbulent mixing,
594   and radiative transfer in the stratocumulus-topped marine boundary layer and comparisons with
595   measurements. *Journal of the atmospheric sciences*, *52*(8), 1204-1236.

596   Ackerman, A. S., Toon, O. B., Stevens, D. E., Heymsfield, A. J., Ramanathan, V., & Welton, E. J. (2000).
597   Reduction of tropical cloudiness by soot. *Science*, *288*(5468), 1042-1047.

598   Ackerman, A. S., Kirkpatrick, M. P., Stevens, D. E., & Toon, O. B. (2004). The impact of humidity above
599   stratiform clouds on indirect aerosol climate forcing. *Nature*, *432*(7020), 1014-1017.

600   Ackerman, A.S., M.C. van Zanten, B. Stevens, V. Savic-Jovcic, C.S. Bretherton, A. Chlond, J.-G. Golaz, H.
601   Jiang, M. Khairoutdinov, S.K. Krueger, D.C. Lewellen, A. Lock, C.-H. Moeng, K. Nakamura,
602   M.D. Petters, J.R. Snider, S. Weinbrecht, and M. Zulauf, 2009: Large-eddy simulations of a
603   drizzling, stratocumulus-topped marine boundary layer. *Mon. Weather Rev., 137*, 1083-1110.

604   Adebiyi, A. A., Zuidema, P., & Abel, S. J. (2015). The convolution of dynamics and moisture with the
605   presence of shortwave absorbing aerosols over the southeast Atlantic. *J. Clim.*, *28*, 1997-2024.

606   Adebiyi, A. A., & Zuidema, P. (2016). The role of the southern African easterly jet in modifying the
607   southeast Atlantic aerosol and cloud environments. *Quarterly Journal of the Royal Meteorological*
608   *Society*, *142*(697), 1574-1589.

609   Albrecht, B. A. (1989). Aerosols, cloud microphysics, and fractional cloudiness. *Science*, *245*(4923), 1227-
610   1230.

611   Bretherton, C. S., & Wyant, M. C. (1997). Moisture transport, lower-tropospheric stability, and decoupling
612   of cloud-topped boundary layers. *Journal of the Atmospheric Sciences*, *54*(1), 148-167.

613   Bretherton, C. S., Blossey, P. N., & Uchida, J. (2007). Cloud droplet sedimentation, entrainment efficiency,
614   and subtropical stratocumulus albedo. *Geophysical Research Letters*, *34*(3).

615   Chand, D., Wood, R., Anderson, T. L., Satheesh, S. K., & Charlson, R. J. (2009). Satellite-derived direct
616   radiative effect of aerosols dependent on cloud cover. *Nature Geoscience*, *2*(3), 181-184.

617   Coakley, J. A., Jr., & Walsh, C. D. (2002). Limits to the aerosol indirect radiative effect derived from
618   observations of ship tracks. *J. Atmos. Sci., 59*, 668-680.

619   Cook, J., & Highwood, E. J. (2004). Climate response to tropospheric absorbing aerosols in an intermediate

620   general-circulation model. *Quarterly Journal of the Royal Meteorological Society*, *130*(596), 175-

621   191.

622   de Lozar, A., and J. Mellado, 2016: Reduction of the entrainment velocity by

623   cloud droplet sedimentation in stratocumulus. *J. Atmos. Sci.* doi:10.1175/JAS-D-

624   16-0196.1, in press.

625   de Roode, S. R., Sandu, I., van der Dussen, J. J., Ackerman, A. S., Blossey, P., Jarecka, D., ... & Stevens,

626   B. (2016). Large eddy simulations of EUCLIPSE/GASS Lagrangian stratocumulus to cumulus

627   transitions: Mean state, turbulence, and decoupling. *Journal of the Atmospheric Sciences*, (2016).

628   Engelhart, G. J., Hennigan, C. J., Miracolo, M. A., Robinson, A. L., & Pandis, S. N. (2012). Cloud

629   condensation nuclei activity of fresh primary and aged biomass burning aerosol. *Atmospheric

630   Chemistry and Physics*, *12*(15), 7285-7293.

631   Feingold, G., Jiang, H., & Harrington, J. Y. (2005). On smoke suppression of clouds in Amazonia.

632   *Geophysical Research Letters*, *32*(2).

633   Forster, A., Schouten, S., Baas, M., & Damsté, J. S. S. (2007). Mid-Cretaceous (Albian–Santonian) sea

634   surface temperature record of the tropical Atlantic Ocean. *Geology*, *35*(10), 919-922.

635   Geoffroy, O., Brenguier, J.-L., & Burnet, F. (2010). Parametric representation of the cloud droplet spectra

636   for LES warm bulk microphysical schemes. *Atmos. Chem. Phys., 10*, 4835-4848.

637   Ghan, S. J. (2013). Technical Note: Estimating aerosol effects on cloud radiative forcing. *Atmospheric

638   Chemistry and Physics, 13*(19), 9971-9974.

639   Hansen, J., Sato, M., & Ruedy, R. (1997). Radiative forcing and climate response. *Journal of Geophysical

640   Research: Atmospheres*, *102*(D6), 6831-6864.

641   Haywood, J., Francis, P., Dubovik, O., Glew, M., & Holben, B. (2003a). Comparison of aerosol size

642   distributions, radiative properties, and optical depths determined by aircraft observations and Sun

643   photometers during SAFARI 2000. *Journal of Geophysical Research: Atmospheres*, *108*(D13).

644   Haywood, J., Osborne, S. R., Francis, P. N., Keil, A., Formenti, P., Andrae, M. O., & Kaye, P. H. (2003b).

645   The mean physical and optical properties of regional haze dominated by biomass burning aerosol

646 measured from the C-130 aircraft during SAFARI 2000. *Journal of Geophysical Research:*
647 *Atmospheres*, *108*(D13).

648 Hindman, E. E., Porch, W. M., Hudson, J. G., & Durkee, P. A. (1994). Ship-produced cloud lines of 13
649 July 1991. *Atmospheric Environment*, *28*(20), 3393-3403.

650 Jacobson, M. Z. (2002). Control of fossil-fuel particulate black carbon and organic matter, possibly the
651 most effective method of slowing global warming. *Journal of Geophysical Research:*
652 *Atmospheres*, *107*(D19).

653 Jayaraman, A., Lubin, D., Ramachandran, S., Ramanathan, V., Woodbridge, E., Collins, W. D., & Zalpuri,
654 K. S. (1998). Direct observations of aerosol radiative forcing over the tropical Indian Ocean during
655 the January-February 1996 pre-INDOEX cruise. *Journal of Geophysical Research: Atmospheres*,
656 *103*(D12), 13827-13836.

657 Johnson, B. T., Shine, K. P., & Forster, P. M. (2004). The semi-direct aerosol effect: Impact of absorbing
658 aerosols on marine stratocumulus. *Quarterly Journal of the Royal Meteorological Society*,
659 *130*(599), 1407-1422.

660 Johnson, B. T. (2005). Large-eddy simulations of the semidirect aerosol effect in shallow cumulus regimes.
661 *Journal of Geophysical Research: Atmospheres*, *110*(D14).

662 Keil, A., & Haywood, J. M. (2003). Solar radiative forcing by biomass burning aerosol particles during
663 SAFARI 2000: A case study based on measured aerosol and cloud properties. *Journal of*
664 *Geophysical Research: Atmospheres*, *108*(D13).

665 Khairoutdinov, M. F., & Randall, D. A. (2003). Cloud resolving modeling of the ARM summer 1997 IOP:
666 Model formulation, results, uncertainties, and sensitivities. *Journal of the Atmospheric Sciences*,
667 *60*(4), 607-625.

668 Klein, S. A., & Hartmann, D. L. (1993). The seasonal cycle of low stratiform clouds. *Journal of Climate*,
669 *6*(8), 1587-1606.Morrison, H., Curry, J. A., & Khvorostyanov, V. I. (2005). A new double-
670 moment microphysics parameterization for application in cloud and climate models. Part I:
671 Description. *Journal of the Atmospheric Sciences*, *62*(6), 1665-1677.

672 Labonne, M., Bréon, F. M., & Chevallier, F. (2007). Injection height of biomass burning aerosols as seen
673 from a spaceborne lidar. *Geophysical Research Letters*, *34*(11).

674 Lindstrot, R., Stengel, M., Schröder, M. Fischer, J., Preusker, R., Steenbergen, T., & Bojkov, B. R. (2014).

675   A global climatology of total columnar water vapour from SSM/I and MERIS. *Earth. Sys. Sci.*

676   *Data, 6*, 221-233.

677 Loeb, N. G., & Schuster, G. L. (2008). An observational study of the relationship between cloud, aerosol

678   and meteorology in broken low-level cloud conditions. *Journal of Geophysical Research:*

679   *Atmospheres*, *113*(D14).

680 Lohmann, U., & Feichter, J. (2001). Can the direct and semi-direct aerosol effect compete with the indirect

681   effect on a global scale?. *Geophysical Research Letters*, *28*(1), 159-161.

682 Menon, S., Hansen, J., Nazarenko, L., & Luo, Y. (2002). Climate effects of black carbon aerosols in China

683   and India. *Science*, *297*(5590), 2250-2253.

684 Morrison, H., Curry, J. A., & Khvorostyanov, V. I. (2005). A new double-moment microphysics

685   parameterization for application in cloud and climate models. Part I: Description. *Journal of the*

686   *Atmospheric Sciences*, *62*(6), 1665-1677.

687 Morrison, H., & Grabowski, W. W. (2008). Modeling supersaturation and subgrid-scale mixing with two-

688   moment bulk warm microphysics. *Journal of the Atmospheric Sciences*, *65*(3), 792-812.

689 Penner, J. E., Zhang, S. Y., & Chuang, C. C. (2003). Soot and smoke aerosol may not warm climate.

690   *Journal of Geophysical Research: Atmospheres*, *108*(D21).

691 Petters, M. D., & Kreidenweis, S. M. (2007). A single parameter representation of hygroscopic growth and

692   cloud condensation nucleus activity. *Atmospheric Chemistry and Physics*, *7*(8), 1961-1971.

693 Pincus, R., & Baker, M. B. (1994). Effect of precipitation on the albedo susceptibility of clouds in the

694   marine boundary layer. *Nature*, *372*(6503), 250-252.

695 Randall, D. A., Coakley Jr, J. A., Lenschow, D. H., Fairall, C. W., & Kropfli, R. A. (1984). Outlook for

696   research on subtropical marine stratification clouds. *Bulletin of the American Meteorological*

697   *Society*, *65*(12), 1290-1301.

698 Sakaeda, N., Wood, R., & Rasch, P. J. (2011). Direct and semidirect aerosol effects of southern African

699   biomass burning aerosol. *Journal of Geophysical Research: Atmospheres*, *116*(D12).

700 Sandu, I., Brenguier, J. L., Geoffroy, O., Thouron, O., & Masson, V. (2008). Aerosol impacts on the

701   diurnal cycle of marine stratocumulus. *Journal of the Atmospheric Sciences*, *65*(8), 2705-2718.

702 Sandu, I., Stevens, B., & Pincus, R. (2010). On the transitions in marine boundary layer cloudiness. *Atmospheric Chemistry and Physics*, *10*(5), 2377-2391.

704 Sandu, I., & Stevens, B. (2011). On the factors modulating the stratocumulus to cumulus transitions. *Journal of the Atmospheric Sciences*, *68*(9), 1865-1881.

706 Satheesh, S. K., & Ramanathan, V. (2000). Large differences in tropical aerosol forcing at the top of the atmosphere and Earth's surface. *Nature*, *405*(6782), 60.

708 Slingo, A., & Schrecker, H. M. (1982). On the shortwave radiative properties of stratiform water clouds. *Quarterly Journal of the Royal Meteorological Society, 108*(456), 407-426.

710 Stevens, B., Cotton, W. R., Feingold, G., & Moeng, C.-H. (1998). Large eddy simulations of strongly precipitating, shallow, stratocumulus-topped boundary layers. *Journal of the Atmospheric Sciences*, *55*, 3616-3638.

713 Toon, O. B., McKay, C. P., Ackerman, T. P., & Santhanam, K. (1989). Rapid calculation of radiative heating rates and photodissociation rates in inhomogeneous multiple scattering atmospheres. *J. Geophys. Res., 94*(D13), 16287-16301.

716 Twomey, S. (1974). Pollution and the planetary albedo. *Atmospheric Environment*, *8*(12), 1251-1256.

717 Twomey, S. (1991). Aerosols, clouds and radiation. *Atmospheric Environment. Part A. General Topics*, *25*(11), 2435-2442.

719 Vogelmann, A.M., A.M. Fridlind, T. Toto, S. Endo, W. Lin, J. Wang, S. Feng, Y. Zhang, D.D Turner, Y. Liu, Z. Li, S. Xie, A.S. Ackerman, M. Zhang, & M. Khairoutdinov (2015). RACORO continental boundary layer cloud investigations. Part I: Case study development and ensemble large-scale forcings. *J. Geophys. Res. Atmos., 120*(12), 5962-5992, doi:10.1002/2014JD022713.

723 Wilcox, E. M. (2010). Stratocumulus cloud thickening beneath layers of absorbing smoke aerosol. *Atmospheric Chemistry and Physics*, *10*(23), 11769-11777.

725 Wyant, M. C., Bretherton, C. S., Rand, H. A., & Stevens, D. E. (1997). Numerical simulations and a conceptual model of the stratocumulus to trade cumulus transition. *Journal of the Atmospheric Sciences*, *54*(1), 168-192.

728 Wood, R. (2007). Cancellation of aerosol indirect effects in marine stratocumulus through cloud thinning. *J. Atmos. Sci. 64*, 2657-2779.

730 Xue, H., Feingold, G., & Stevens, B. (2008). Aerosol effects on clouds, precipitation, and the organization

731   of shallow cumulus convection. *Journal of the Atmospheric Sciences*, *65*(2), 392-406.

732 Yamaguchi, T., Feingold, G., Kazil, J., & McComiskey, A. (2015). Stratocumulus to cumulus transition in

733   the presence of elevated smoke layers. *Geophysical Research Letters*, *42*(23).

734 Zhou, X., Kollias, P., & Lewis, E. R. (2015). Clouds, precipitation, and marine boundary layer structure

735   during the MAGIC field campaign. *Journal of Climate*, *28*(6), 2420-2442.
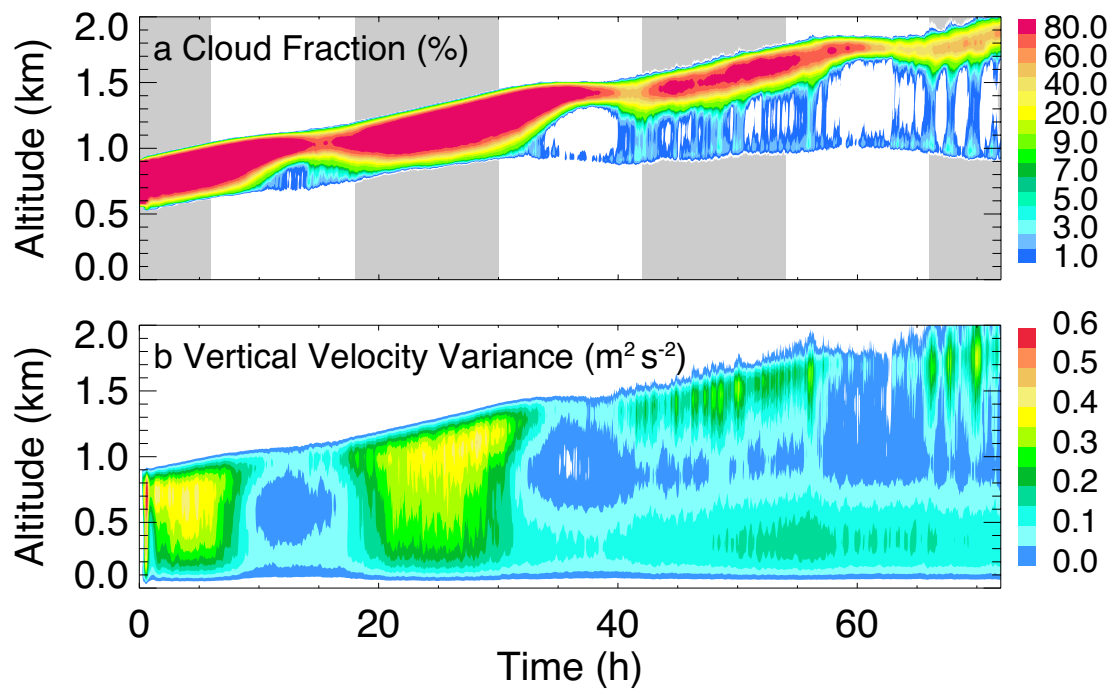
Fig. 1. Evolution of horizontal average profiles of (a) cloud fraction (defined by cloud water mixing ratio threshold of 0.01 g kg^{-1}) and (b) vertical velocity variance for lightly drizzling baseline case ($N_{a, sulfate}$=150 mg^{-1}). The simulation starts at midnight local time. Gray shading indicates nominal nighttime (6 pm~6 am local time).
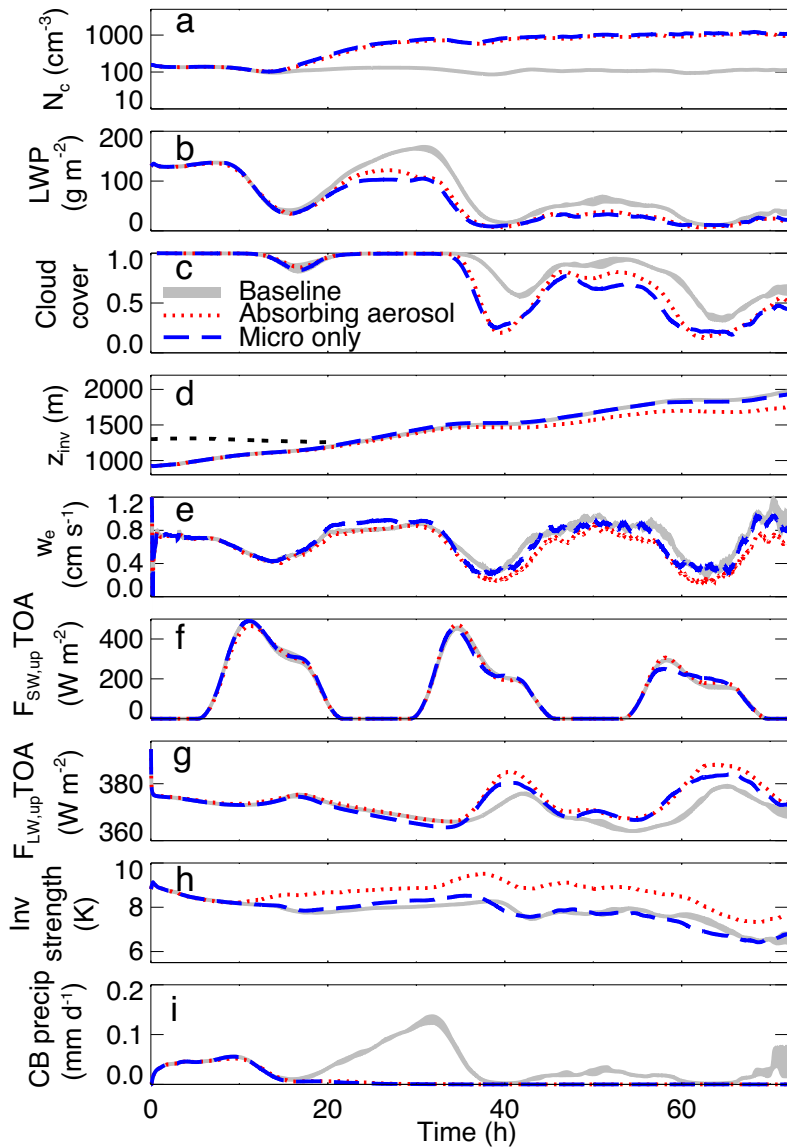
Fig. 2. Evolution of domain averages of (a) cloud droplet number concentration (N_c, average weighted by cloud water mixing ratio), (b) liquid water path (LWP), (c) cloud cover (columns with LWP > 10 g m^{-2}), (d) inversion height (height of maximum potential temperature gradient), (e) entrainment rate (difference of inversion height tendency and subsidence rate at inversion height), (f) upwelling shortwave (SW) and (g) longwave (LW) radiative fluxes at TOA, (h) inversion strength (ΔT across inversion defined as the vertical extent with continuous positive temperature gradient), and (i) precipitation rate at

cloud base (mean over cloudy columns of lowermost height where cloud water mixing ratio exceeds 0.01 g kg^{-1}) . Results shown as lagged 3-hour running averages to smooth entrainment rates. Range of three-member lightly drizzling baseline ensemble ($N_{a, \text{sulfate}} =$ 150 mg^{-1}) in gray. Results with absorbing aerosol layer shown as red dotted line. Results with aerosol layer excluding radiative interaction shown as blue dashed line. The black dotted line in (d) indicates the base of absorbing aerosol layer (lowest height where $N_{a, \text{absorb}}$ is full strength) before contacting the boundary layer.
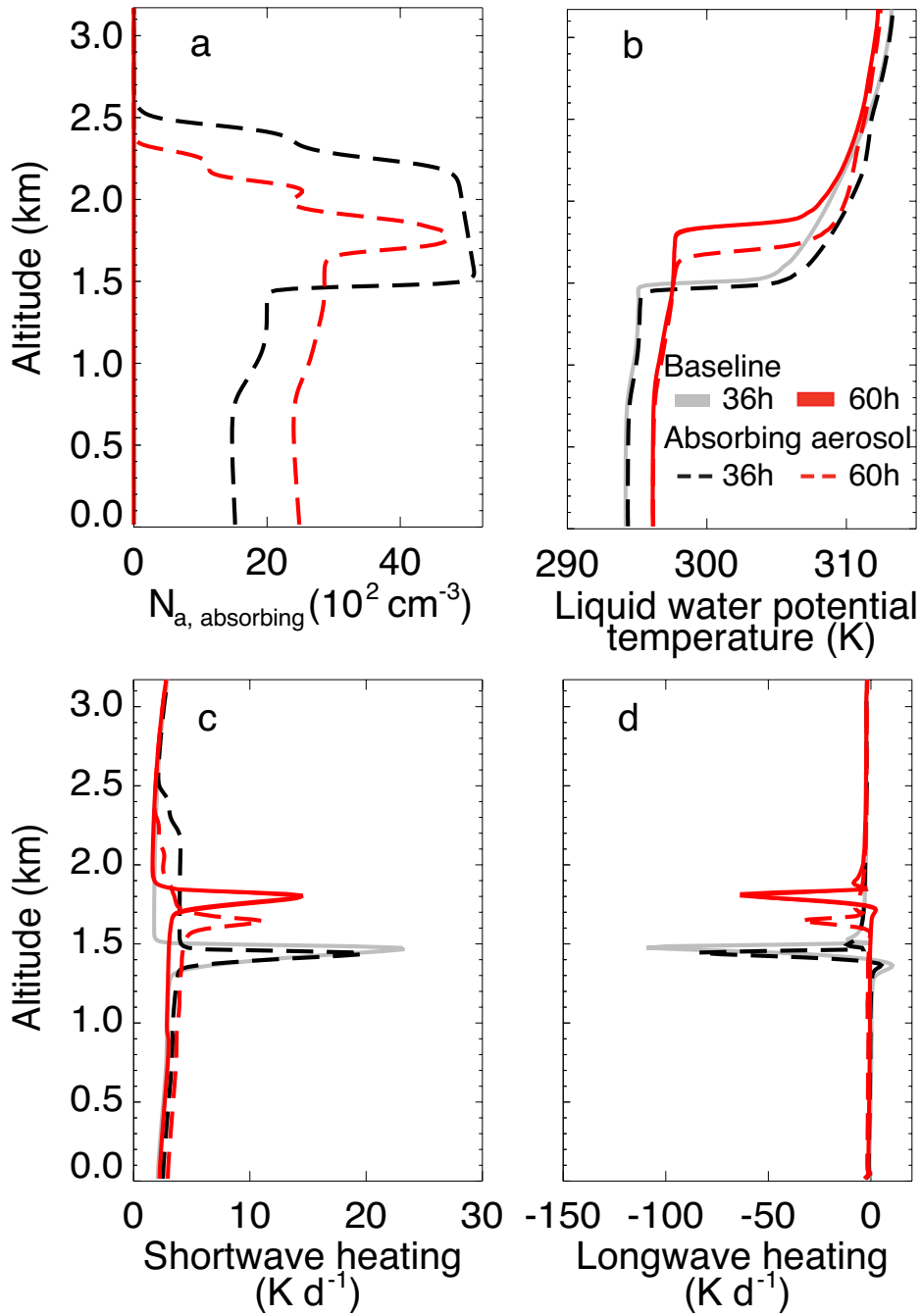
Fig. 3. Horizontally averaged profiles of (a) number concentration of absorbing aerosol, (b) liquid water potential temperature, (c) SW heating rate and (d) LW heating rate at 36th hour (gray solid line) and 60th hour (red solid line) for lightly drizzling baseline ensemble ($N_{a, sulfate}$ = 150 mg^{-1}) and with overlying absorbing aerosol (dashed line).
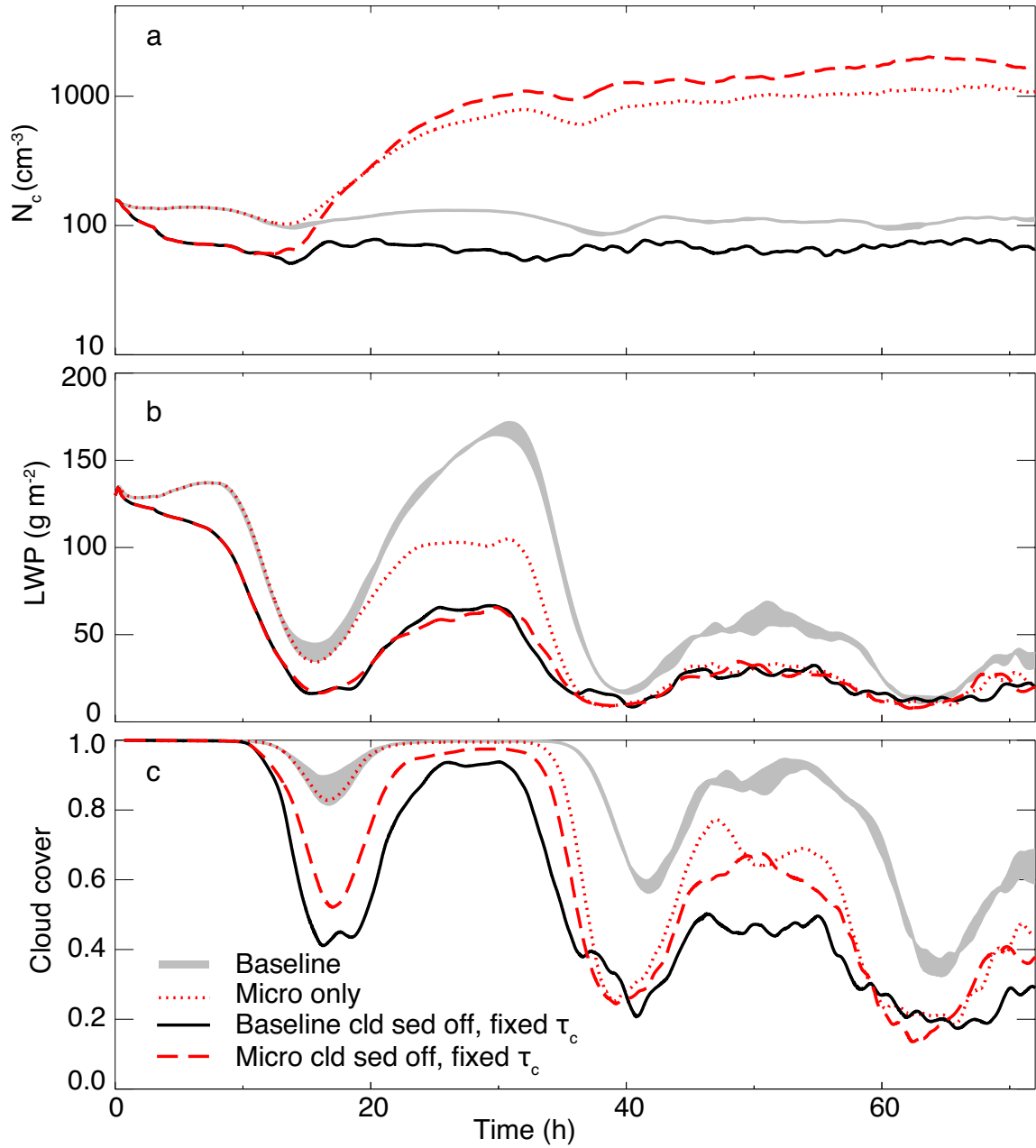
Fig. 4. As in Fig. 2 with baseline in gray and with overlying aerosol that does not affect radiation shown with dotted red line. Baseline and overlying aerosol cases in the absence of cloud-droplet sedimentation and with fixed relaxation time for diffusional growth of cloud droplet (τ_c) are shown with black solid and red dashed lines respectively.
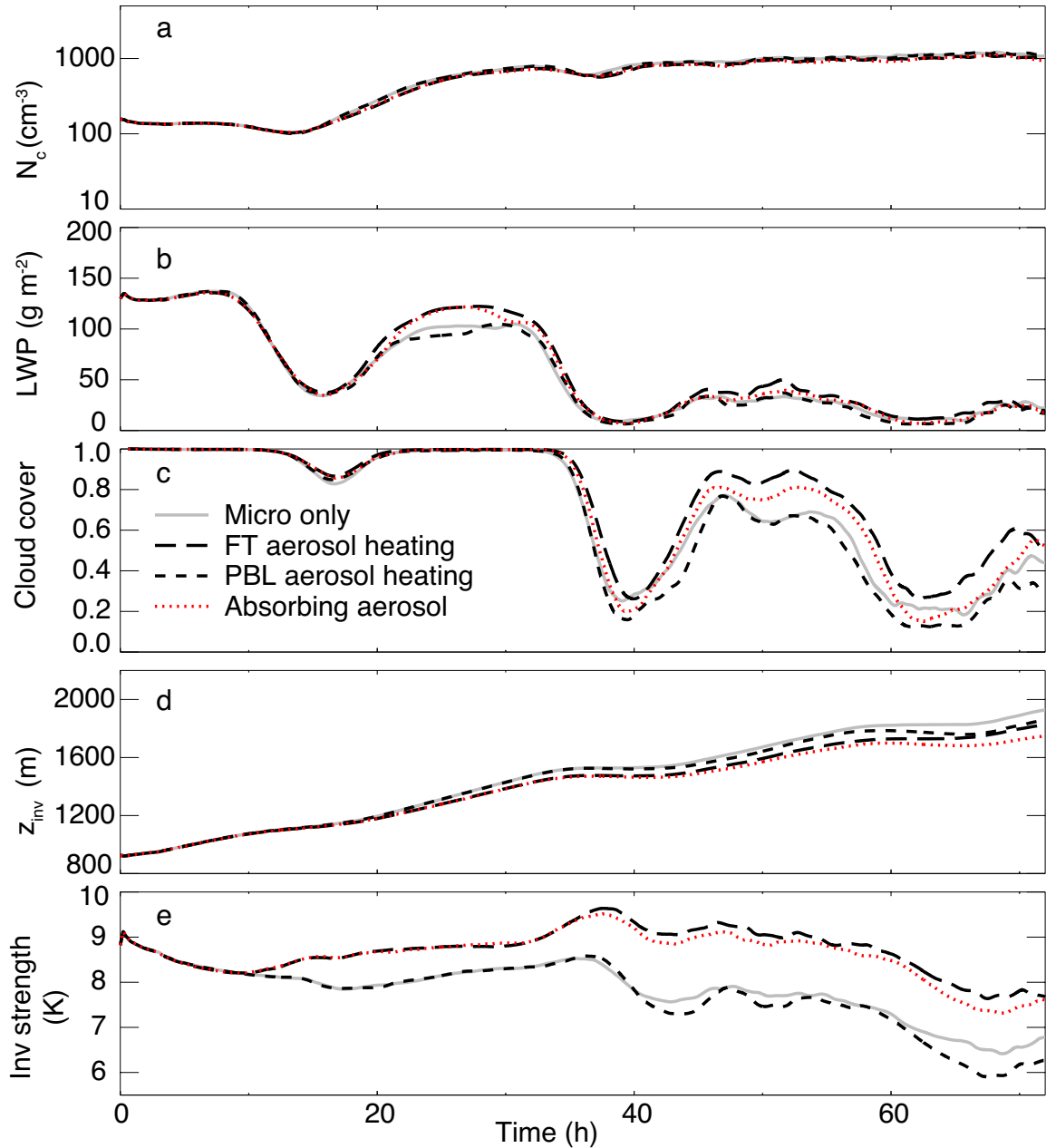
Fig. 5. As in Fig. 2. All cases include initially overlying absorbing aerosol and allow them to act as CCN. For gray solid line the aerosol does not affect radiation. For long and short dashed lines, the aerosol affects radiation only in the free troposphere (FT) and planetary boundary layer (PBL), respectively. For red dotted line there are no restrictions on aerosol affecting radiation, as in Fig. 2.
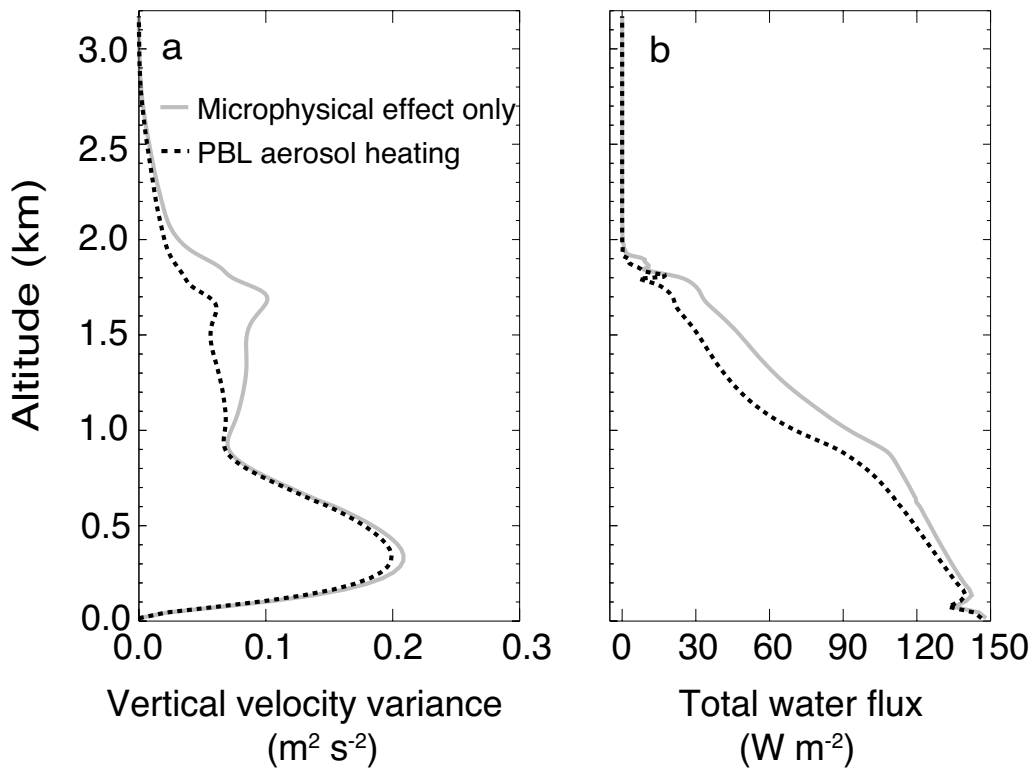
Fig. 6. Horizontally averaged profiles of (a) vertical velocity variance and (b) total water flux averaged over 10 AM to 2 PM local time on day 3 for simulations with (gray solid line) and without (black dotted line) absorbing aerosol affecting radiation in the PBL. Both simulations include microphysical effects of entrained aerosol layer.
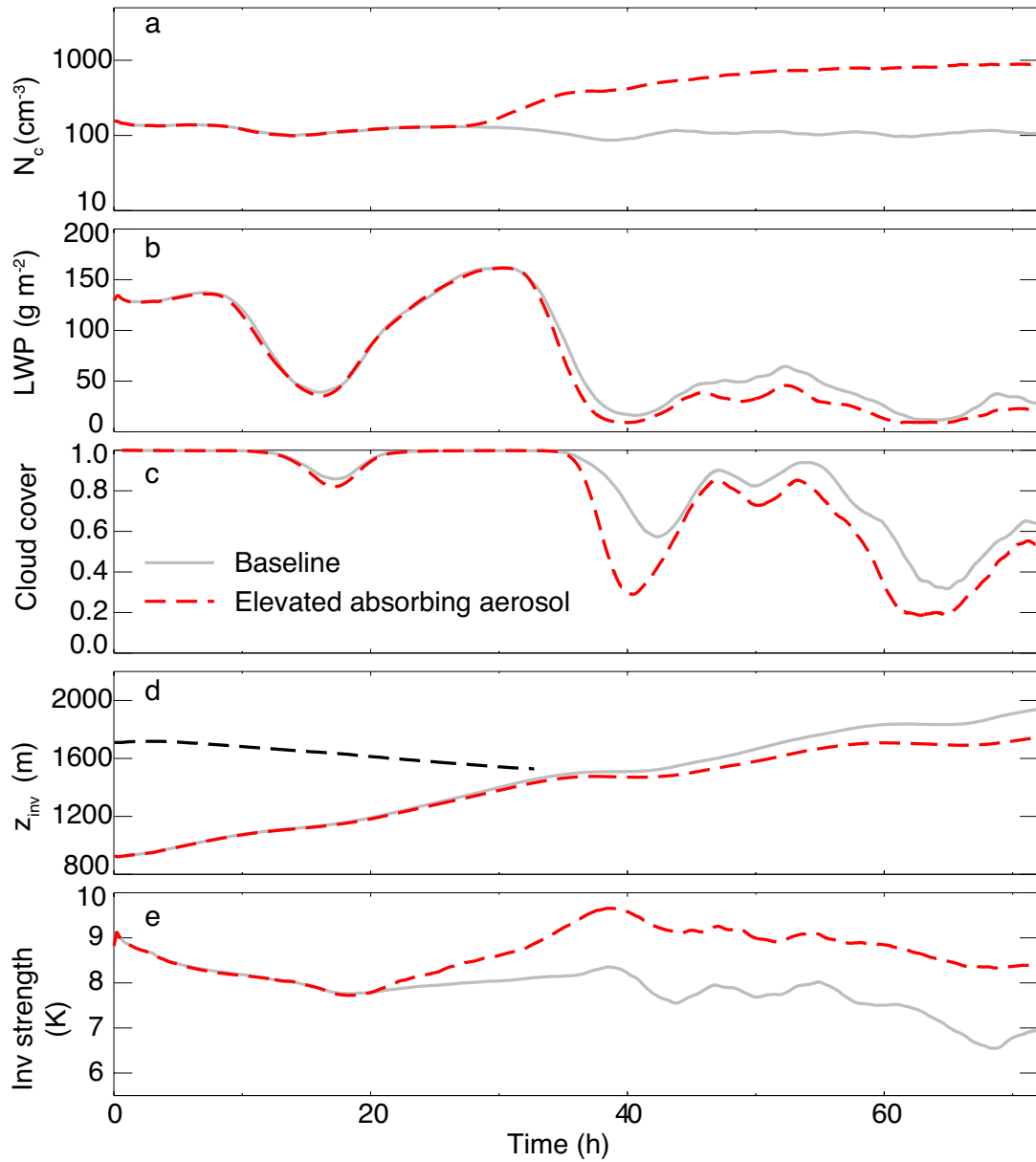
Fig. 7. As in Fig. 2. The baseline with a 3.5-km deep grid ($N_{a,\ sulfate} = 150$ mg^{-1}) shown as gray solid line. Results with aerosol layer initially 400 m higher shown as red dashed line, with corresponding aerosol layer base shown as black dashed line in (d).
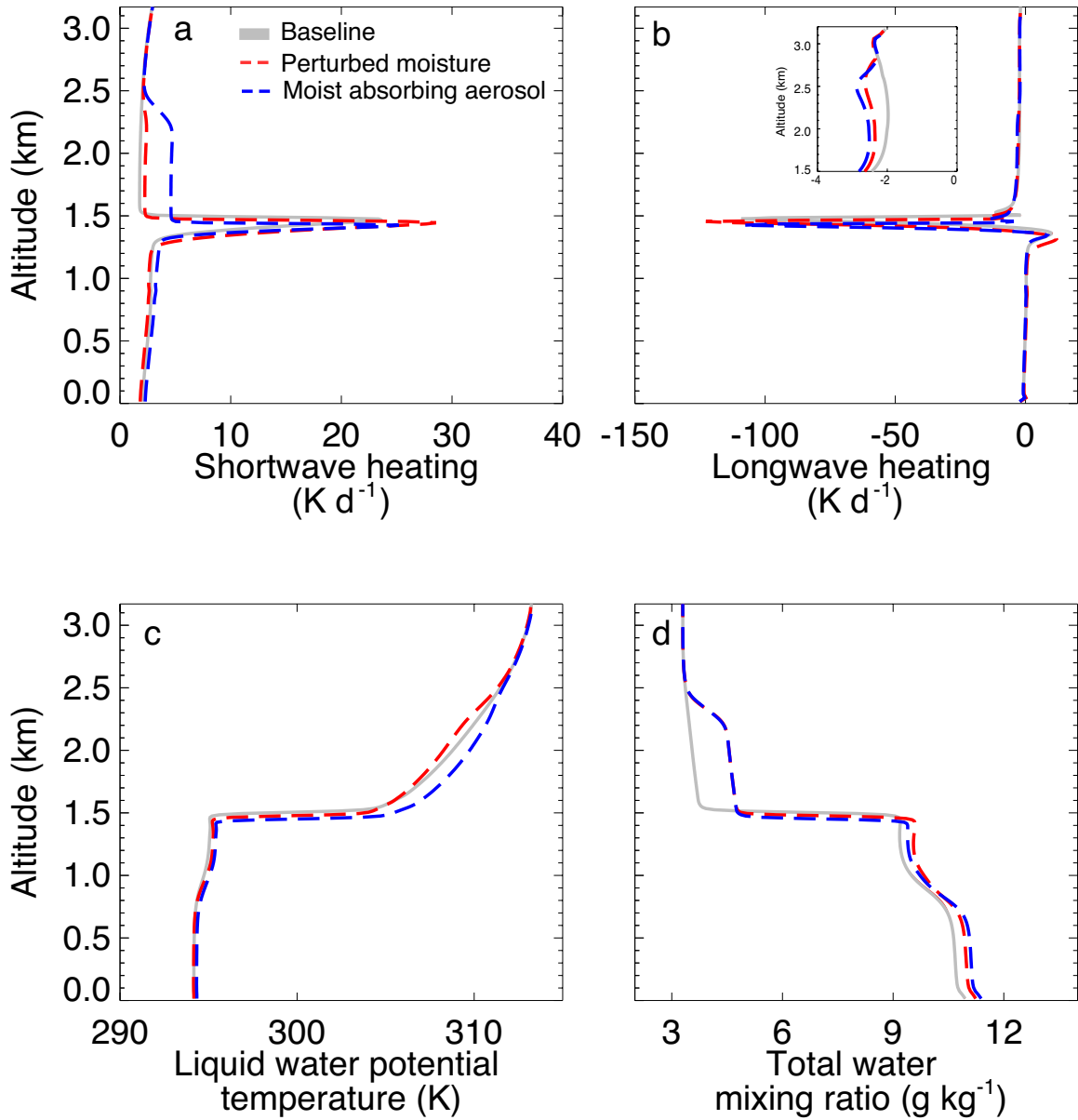
Fig. 8. Horizontally averaged profiles of (a) SW heating rate, (b) LW heating rate, (c) liquid water potential temperature, and (d) total water mixing ratio averaged over hours 35-37 for lightly drizzling baseline ensemble ($N_{a, \text{ sulfate}} = 150$ mg^{-1}) (gray and black), perturbed moist case (red), and perturbed moist absorbing aerosol case (blue). The sub panel in (b) shows diurnal-average LW heating rate profile on day 1 from 1.5 to 3.2 km.
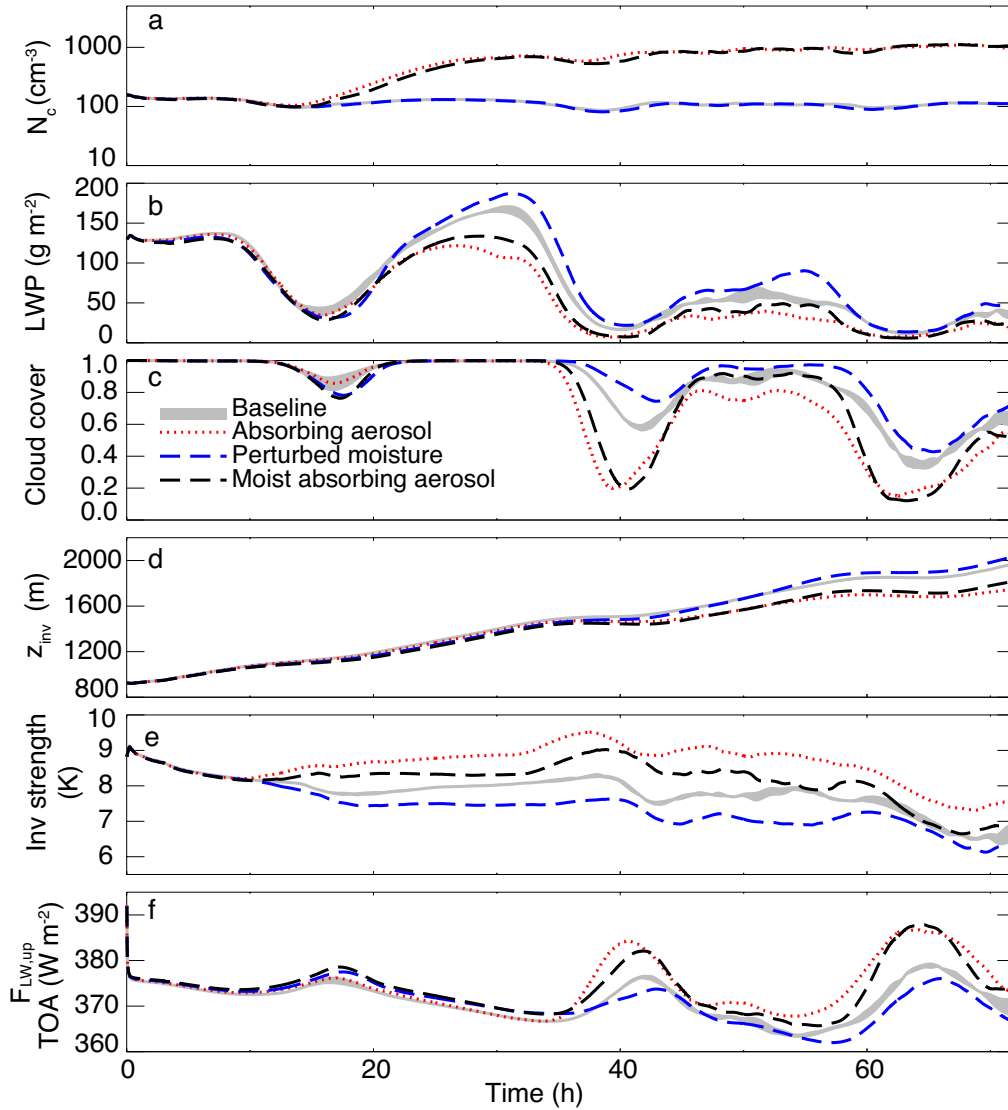
Fig. 9. As in Fig. 2. Range of three-member lightly drizzling baseline ensemble ($N_{a, \text{sulfate}} = 150$ mg^{-1}) shown in gray. Results with absorbing aerosol layer shown as red dotted line. Baseline with moist layer aloft shown as blue dashed line. Results with moist absorbing aerosol shown as black dashed line.
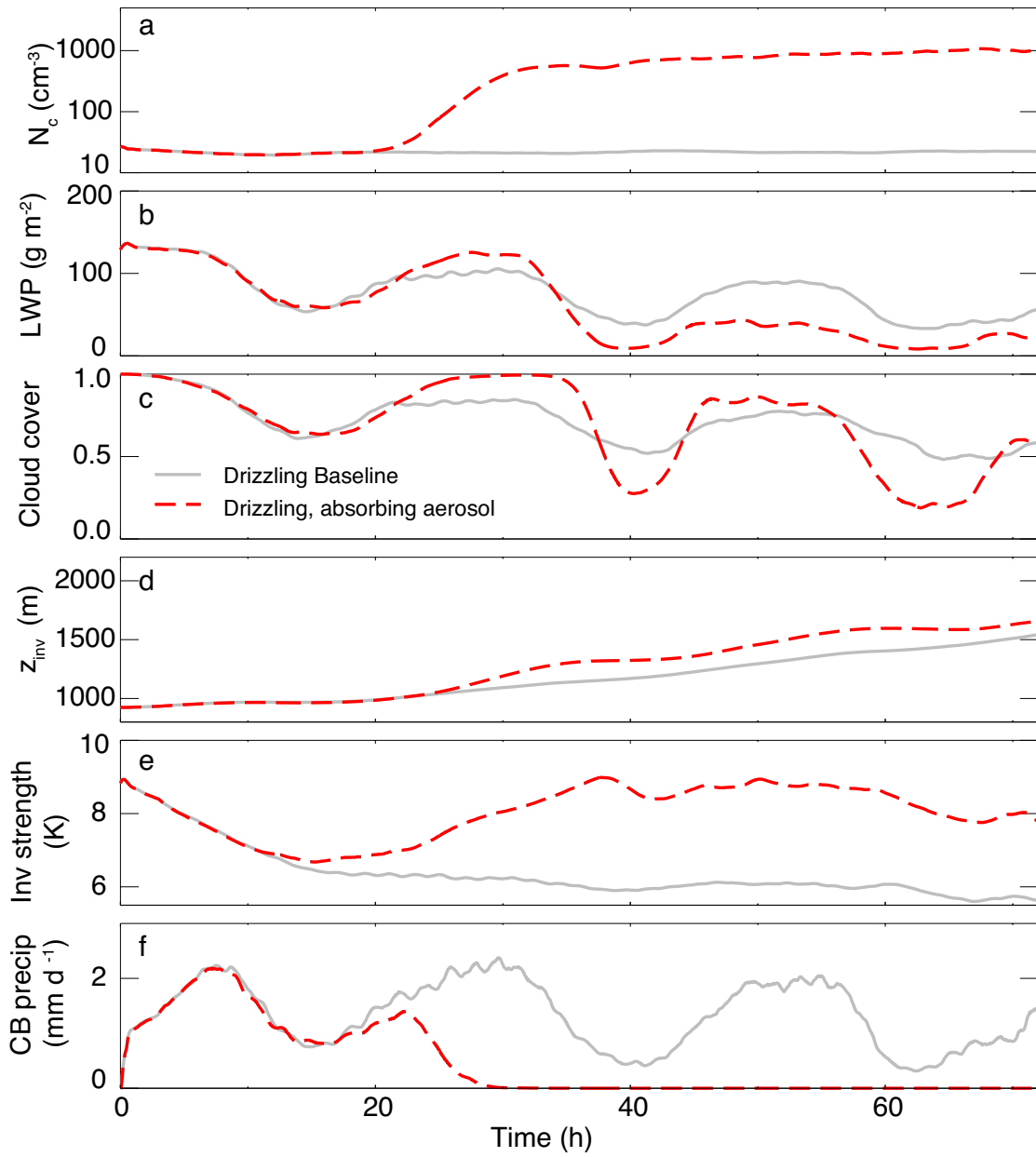
Fig. 10. As in Fig. 2 but for heavily drizzling baseline ($N_{a, \text{sulfate}} = 25$ mg^{-1}).
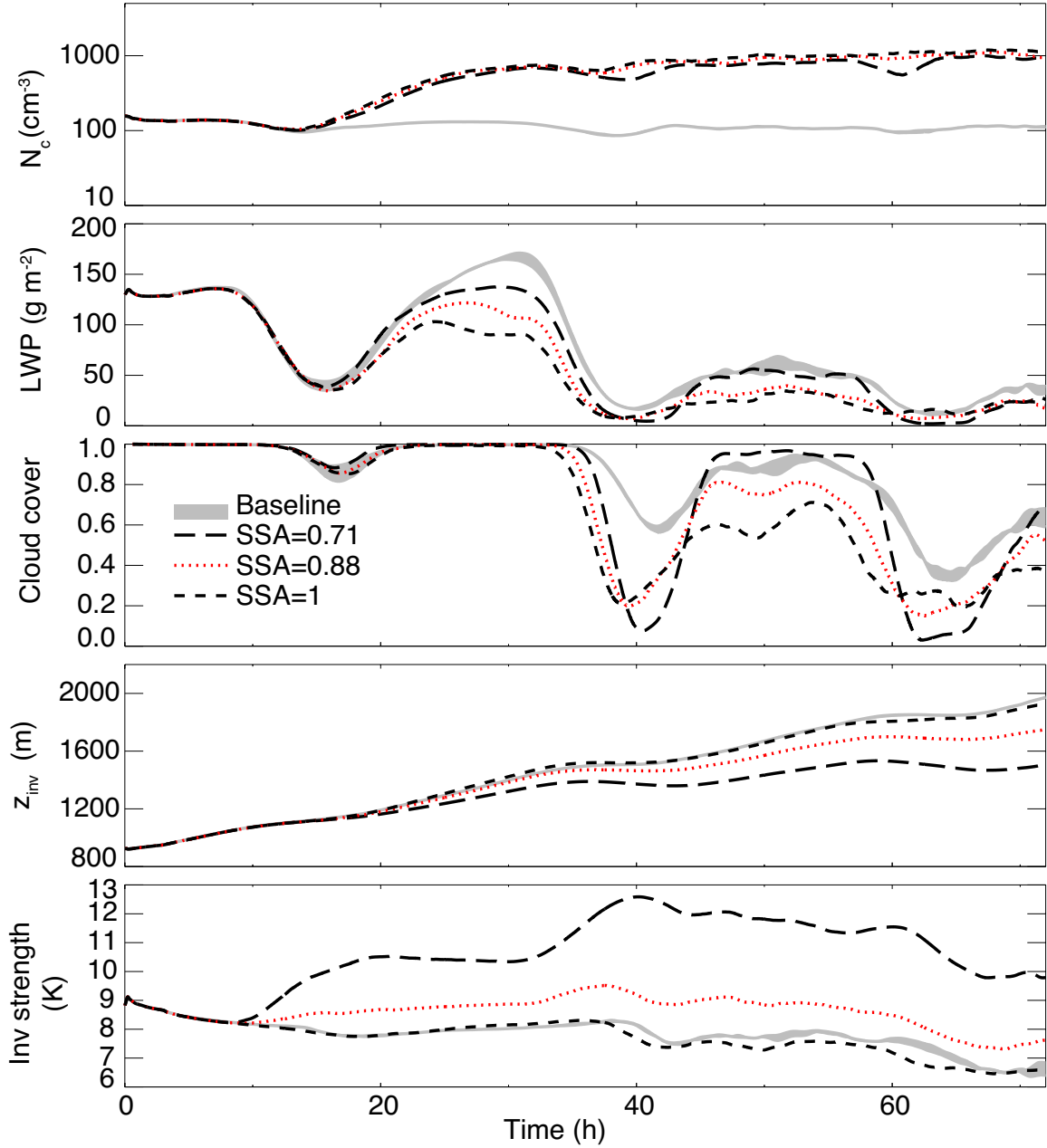
Fig. A1. As in Fig. 2. Range of three-member lightly drizzling baseline ensemble ($N_{a,\ sulfate}$ = 150 mg^{-1}) in gray. Varying single scattering albedo (SSA) of absorbing aerosol as given in legend.
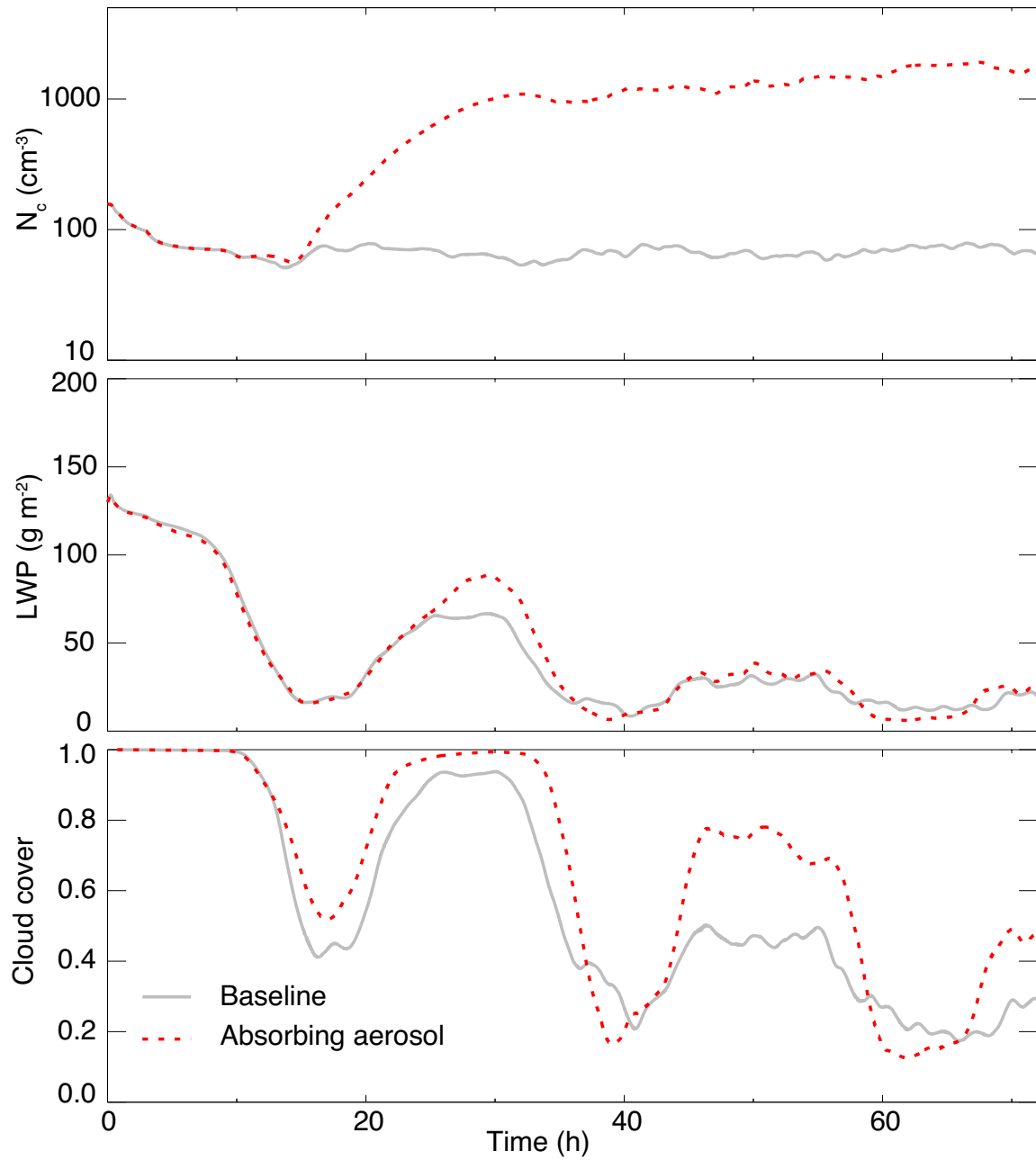
Fig. A2. As in Fig. 2 but for lightly drizzling baseline and with absorbing aerosol in the absence of sedimentation and evaporation effects.

TABLES

Table 1. Summary of simulation setups. See text for details.

	Ammonium sulfate $N_{a,\,sulfate}=150$ (mg^{-1})	Absorbing aerosol $N_{a,\,absorb}=5000$ (mg^{-1})					Cloud droplet sedimentation	Prognostic relaxation time for diffusional growth	Figure(s)
		At 1300 (m)	Additional moisture of 1 g kg^{-1}	Micro-physics	FT Aerosol heating	PBL Aerosol heating			
Baseline	√	√	-	-	-	-	√	√	1,2,3,4,7,8,9
Absorbing aerosol	√	√	-	√	√	√	√	√	2,3,5,9
Micro only	√	√	-	√	-	-	√	√	2,4,5,6
Baseline cld sed off, fixed τ_c	√	√	-	-	-	-	-	-	4
Micro cld sed off, fixed τ_c	√	√	-	√	√	√	-	-	4
FT aerosol heating	√	√	-	√	√	-	√	√	5
PBL aerosol heating	√	√	-	√	-	√	√	√	5,6
Elevated absorbing aerosol	√	1700	-	√	√	√	√	√	7
Perturbed moisture	√	-	√	-	-	-	√	√	8,9
Moist absorbing aerosol	√	√	√	√	√	√	√	√	8,9
Drizzling baseline	25	√	-	-	-	-	√	√	10
Drizzling, absorbing aerosol	25	√	√	√	√	√	√	√	10

Table 2. Diurnal-average direct forcing, indirect plus semi-direct forcing, and sum of forcings (in W m^{-2}) from the overlying absorbing aerosol for the lightly drizzling case ($N_{a,\ sulfate}$ = 150 mg^{-1}) on day 1 (0-24 h), day 2 (24-48 h) and day 3 (48-72 h). The three-day average radiative forcing is indicated in the last row. Boldface indicates results exceeding the uncertainty range derived from the baseline ensemble spread.

	Direct forcing			Indirect + semi-direct forcing			Total
	SW	LW	SW+LW	SW	LW	SW+LW	SW+LW
Day 1	**7.3**	**-0.3**	7.0	-1.6	**-0.2**	-1.8	**5.2**
Day 2	**0.8**	**-0.2**	0.6	-0.5	**-2.6**	**-3.1**	-2.5
Day 3	**-3.7**	0.0	**-3.7**	**-1.2**	**-6.0**	-7.2	-10.9
Mean	1.5	**-0.2**	1.3	-1.1	**-2.9**	**-4.0**	**-2.7**

Table 3. Diurnal-average changes in cloud radiative forcings (ΔCRF; in W m^{-2}) for the overlying absorbing aerosol case relative to the lightly drizzling baseline case ($N_{a, \text{sulfate}} = 150$ mg^{-1}). Conventions as in Table 2.

	ΔCRF TOA (W m^{-2})		
	SW	LW	SW+LW
Day 1	**14.6**	-0.2	**14.4**
Day 2	**8.5**	**-2.0**	**6.5**
Day 3	**2.3**	**-4.8**	**-2.5**
Mean	**8.4**	**-2.3**	**6.1**

Table 4. Indirect forcing of absorbing aerosol, computed as the diurnal-average difference in radiative fluxes at TOA (in W m^{-2}) of the simulation with absorbing aerosol not directly affecting radiation, relative to the lightly drizzling baseline case ($N_{a, sulfate}$ = 150 mg^{-1}). Conventions as in Table 2.

	Indirect forcing		
	SW	LW	SW+LW
Day 1	-0.7	**0.4**	-0.3
Day 2	**2.5**	**-0.9**	**1.6**
Day 3	**1.2**	**-5.2**	**-4.0**
Mean	1.0	**-1.9**	-0.9

Table 5. Schematic of SW and LW radiative responses (changes in net downward fluxes at TOA) to microphysical and thermal effects of initially overlying absorbing aerosol layer. N_c refer to cloud-droplet concentrations, CF cloud fraction, and Z_i inversion height. Plus signs refer to positive responses, negative signs to negative responses, and zeros to negligible or absent responses.

		SW	LW
Microphysical effects			
Twomey effect	N_c⬆	-	0
Cloud-droplet sedimentation ⬇, evaporation⬆	CF⬇	+	-
FT aerosol heating			
Inversion strength⬆	CF⬆	-	+
	Z_i⬇	0	-
PBL aerosol heating			
RH decrease	CF⬇	+	-
	Z_i⬇	0	-
Other			
Warming SST		0	-

Table 6. Semi-direct forcing of absorbing aerosol, computed as the diurnal-average difference in radiative fluxes at TOA (in W m^{-2}) of simulations with aerosol heating restricted to the FT, PBL, or not restricted, relative to the simulation without aerosol heating. All simulations allow the absorbing aerosol to act as CCN. Boldface indicates results exceeding the uncertainty range derived from the spread of the lightly drizzling baseline ensemble.

		Semi-direct forcing		
		SW	LW	SW+LW
FT aerosol heating	Day 1	-1.9	**-0.6**	-2.5
	Day 2	**-12.4**	**-0.2**	**-12.6**
	Day3	**-20.6**	**2.7**	**-17.9**
PBL aerosol heating	Day 1	-1.3	0.0	-1.3
	Day 2	**5.5**	**-1.2**	**4.3**
	Day3	**15.2**	**-3.2**	**12.0**
	Day 1	-0.9	**-0.6**	-1.5
FT, PBL aerosol heating	Day2	**-3.0**	**-1.7**	**-4.7**
	Day3	**-2.4**	**-0.8**	**-3.2**
	Mean	**-2.1**	**-1.0**	**-3.1**

Table 7. As in Table 2 but with absorbing aerosol layer initially located 400 m higher. Boldface indicates results exceeding the uncertainty range derived from the spread of the lightly drizzling baseline ensemble.

	Direct forcing			Indirect + semi-direct forcing			Total
	SW	LW	SW+LW	SW	LW	SW+LW	SW+LW
Day 1	**6.5**	**-0.2**	**6.3**	4.2	**-0.6**	3.6	**9.9**
Day 2	**3.8**	**-0.3**	**3.5**	**-11.2**	**-1.9**	**-13.1**	**-9.6**
Day 3	**-3.0**	-0.1	**-3.1**	**-5.0**	**-4.7**	**-9.7**	**-12.8**
Mean	**2.4**	**-0.2**	**2.2**	**-4.0**	**-2.4**	**-6.4**	**-4.2**

Table 8. As in Table 2 but for the response of a lightly drizzling baseline to a perturbation of moisture instead of aerosol. Boldface indicates results exceeding the uncertainty range derived from the spread of the lightly drizzling baseline ensemble.

	Net flux change at TOA (W m^{-2})		
	SW	LW	SW+LW
Day 1	**11.6**	**-1.3**	**10.3**
Day 2	**-17.5**	**-0.2**	**-17.7**
Day 3	**-9.9**	**2.4**	**-7.2**
Mean	**-5.2**	**0.3**	**-4.9**

Table 9. As in Table 2 but for a lightly drizzling baseline with a moisture perturbation aloft. Boldface indicates results exceeding the uncertainty range derived from the spread of the lightly drizzling baseline ensemble.

	Direct forcing			Indirect + semi-direct forcing			Total
	SW	LW	SW+LW	SW	LW	SW+LW	SW+LW
Day 1	**6.1**	**-0.2**	**5.9**	-1.5	**-0.3**	-1.8	4.1
Day 2	**1.8**	**-0.2**	**1.6**	**3.0**	**-2.2**	**0.8**	**2.4**
Day 3	**-3.5**	0.0	**-3.6**	**2.8**	**-6.8**	**-4.0**	**-7.6**
Mean	1.5	-0.1	1.4	1.4	**-3.1**	**-1.7**	-0.3

Table 10. As in Table 9 but for a heavily drizzling baseline ($N_{a,\,sulfate}$=25 mg^{-1}).

	Direct forcing			Indirect + semi-direct forcing			Total
	SW	LW	SW+LW	SW	LW	SW+LW	SW+LW
Day 1	0.3	-0.1	0.2	-0.5	0.0	-0.5	-0.3
Day 2	**2.0**	**-0.2**	**1.8**	**-52.0**	**6.3**	**-45.7**	**-43.9**
Day 3	**-3.4**	**-0.0**	**-3.4**	**-9.4**	**3.4**	**-6.0**	**-9.4**
Mean	-0.4	-0.1	-0.5	**-20.6**	**3.2**	**-17.4**	**-17.9**

Table A1.   As in Table 2 but for absorbing aerosol with different values of single scattering albedo (SSA), and only showing averages over the three-day transition. For the last case the aerosol loading is reduced five-fold.

$N_{a, absorb}$ (mg^{-1})		Direct forcing			Indirect + semi-direct forcing			Total
		SW	LW	SW+LW	SW	LW	SW+LW	SW+LW
	SSA=0.71	**15.9**	**-0.2**	**15.7**	**-5.1**	**-5.2**	**-10.3**	**5.4**
5000	SSA=0.88	**1.5**	**-0.2**	**1.3**	**-1.1**	**-2.9**	**-4.0**	**-2.7**
	SSA=1.00	**-4.9**	**-0.1**	**-5.0**	**0.8**	**-2.5**	**-1.7**	**-6.7**
1000	SSA=0.88	0.2	0.0	0.2	**2.5**	**-1.9**	0.6	0.8